Intrinsic Cellular Persistent Firing Sustains Hippocampal Spatial Representations during Working Memory

Babak Saber Marouf [1 2 3], Antonio Reboreda [2 3], Frederik Theissen [2 3], Rahul Kaushik [4], Magdalena Sauvage [3 5 6], Alexander Dityatev [4 5 6], Motoharu Yoshida [2 3 6]

Affiliations

[1]Institute of Physiology, Medical Faculty, Otto-Von-Guericke University, 39120 Magdeburg, Germany.

[2]Cognitive Neurophysiology, German Center for Neurodegenerative Diseases (DZNE), 39120 Magdeburg, Germany.

[3]FAM Department, Leibniz Institute for Neurobiology (LIN), 39118 Magdeburg, Germany.

[4]Molecular Neuroplasticity Group, German Center for Neurodegenerative Diseases (DZNE), 39120 Magdeburg, Germany.

[5]Medical Faculty, Otto-von-Guericke University (OVGU), 39120 Magdeburg, Germany.

[6]Center for Behavioral Brain Sciences (CBBS), 39106 Magdeburg, Germany.

Abstract

Neurons are the fundamental units of cognitive processing. The prevailing view holds that neurons are input-output units that fire action potentials only upon receiving sufficient synaptic input. Here, we demonstrate that this may not be the sole operational mode of neurons *in vivo* during cognitive tasks, by showing that hippocampal place cells actively maintain firing and preserve spatial information through molecularly defined intrinsic mechanisms. Using *in vitro* and *in vivo* recordings coupled with molecular manipulation in mice, we reveal that hippocampal persistent firing during spatial working memory is supported by individual neurons via TRPC4 ion channels. Despite the general belief that persistent activity carries working memory content, we demonstrate that this firing maintains immediate spatial representations and is required for spatial working memory performance. These findings redefine neurons as active contributors to information retention, beyond their traditional role as passive input-output units, potentially reshaping our general understanding of computation in the brain.

Introduction

Precise maintenance of internal representations in the brain is critical for executing cognitive tasks[1,2]. A potential cellular correlate for this process is persistent neural firing, in which information is maintained by continuous activation of a specific subset of cells[3,4]. Persistent firing has been observed across multiple brain regions, including the prefrontal cortex, hippocampus and sensory association areas, and is thought to support a wide range of cognitive functions such as working memory, decision-making, attention, spatial navigation, and goal-directed behavior[5–10,2]. In the rodent hippocampus, in addition to "time cells" that activate sequentially during relatively short delay intervals (~10 s)[11,12], a recent study has identified persistently firing cells that span the entire delay period (~30 s) in the mouse hippocampal CA1, outlasting the time-cell sequence[13].

Building on the foundational concepts of Lorente de Nó and Hebb, persistent activity has traditionally been attributed to reverberatory dynamics within recurrent synaptic networks[14,15]. This view aligns with the prevailing model of neurons as passive elements generating action potentials only when synaptic inputs exceed a threshold. However, these pure network models often exhibit instabilities such as noise-induced drift and runaway excitation[3], and their performance depends on a degree of synaptic fine-tuning rarely observed in biological systems[4,16]. Consequently, such models often struggle to replicate the robust, long-lasting persistent firing observed in biological systems without incorporating additional stabilizing mechanisms[17].

Neuromodulators such as acetylcholine, which is vital for working memory and other cognitive functions, can transform the way neurons respond to input signals[18]. *In vitro* studies have indicated that individual neurons can continue firing after a brief trigger under the influence of acetylcholine through an intrinsic cellular mechanism—a phenomenon referred to here as “intrinsic persistent firing”[19–24]. We and others have identified TRPC channels as key mediators of intrinsic persistent firing in CA1 pyramidal cells[20,25]. Theoretical studies have demonstrated potential roles for this cellular property in working memory and spatial coding[26,27]. Indeed, incorporating mechanisms of intrinsic persistent firing endows attractor network models with the high stability and robustness observed in *in vivo* data[28–30]. However, whether intrinsic persistent firing influences *in vivo* neural activity, sustains information, and

supports cognitive function remains unclear because the effects of disrupting this property have not been examined in living animals[31,32]. As a consequence, current computational models—from classical attractor networks to the artificial neural networks underlying deep learning—largely rely on synaptic connectivity to sustain activity.

Beyond cellular mechanisms, the specific functional contribution of the hippocampus to spatial working memory remains a subject of intense debate. It has long been contested whether the hippocampus supports spatial working memory by maintaining task-specific content (working memory hypothesis) or by supplying an ongoing spatial representation (cognitive map theory)[33,34]. While human studies repeatedly indicate that hippocampal persistent firing encodes working memory content[8], decoding analyses from the rodent hippocampus have shown an absence of working memory content (e.g. left vs right turns) during the delay period[13,35,36]. Thus, the information represented by hippocampal persistent firing during spatial working memory still remains unclear. Notably, both working memory maintenance and spatial representation have been modeled using similar attractor-based dynamics[37,38] , indicating that the maintenance of head direction or spatial information is associated with persistent firing[39,40]. However, whether the maintenance of spatial representations *in vivo* relies on network-level connectivity or individual cellular mechanisms remains to be determined.

Here, we test the contribution of intrinsically generated persistent firing to the maintenance of internal representations *in vivo* and to cognitive performance. We first identify the TRPC4 ion channel as a molecular mechanism underlying intrinsic persistent firing and subsequently examine neural activity in mice during a spatial working memory task under TRPC4 knockdown (KD). Persistent firing observed in control animals during the delay period of the task was markedly reduced in TRPC4 KD mice, indicating that intrinsic cellular mechanisms support persistent firing *in vivo*. Notably, the transient activity of cells before and after the delay period was not altered, highlighting the specific role of TRPC4 channels in sustained firing. Spatial working memory performance was significantly impaired, providing the first evidence for a functional role of hippocampal persistent firing in this task. Using support vector machine (SVM) decoding and spatial information measurements, we reveal that hippocampal persistent firing reflects the sustained activity of place cells with high spatial information when animals remain at fixed locations (the start and goal areas) for extended periods. Furthermore,

using Bayesian decoding and SVM-based classification, we demonstrate that spatial representation errors increased rapidly and that left–right goal prediction deteriorated upon entry into the goal areas in TRPC4 KD mice, indicating impaired maintenance of spatial representations. Notably, the strength of persistent firing at the goal locations correlated with task performance. These data suggest that hippocampal persistent activity supports spatial working memory by maintaining instantaneous spatial representations. These results position individual neurons as active units of information retention, beyond their traditional role as passive input–output units, and offer a revised framework for understanding memory and neural computation.

Results

TRPC4 KD suppresses intrinsic persistent firing *in vitro*

We developed an shRNA TRPC4 channel knockdown (TRPC4 KD) virus and a control virus with a scrambled sequence (Scrambled) to test the role of intrinsic persistent firing *in vivo* (see Methods; Fig. 1A)[41]. The mice received bilateral injections of either virus into the CA1 region (Fig. 1B). First, a loss of intrinsic persistent firing was confirmed using *in vitro* patch-clamp recordings of hippocampal CA1 cells in the presence of the cholinergic receptor agonist carbachol[20,25] (10 μM; Fig. 1C). Percentages of cells responded with persistent firing, the frequency of persistent firing and membrane depolarization were significantly lower in the TRPC4 KD group than in the two control groups (Fig. 1D-F). Basic properties of TRPC4 KD cells, such as the resting membrane potential, input resistance, adaptation index, and intrinsic excitability, did not significantly differ from those in the control groups (except for intrinsic excitability measured with 100 pA current injection, Kruskal–Wallis test, $p = 0.0193$, Chi-sq $= 7.89$, df $= 2$; Table 1). In summary, TRPC4 KD significantly decreased the ability of individual cells to support persistent firing while preserving basic cellular properties.

TRPC4 KD impairs spatial working memory

Second, the effect of TRPC4 KD on spatial working memory was assessed by a delayed non-match-to-sample paradigm using an automated T-maze (Fig. 1G-I; Supplemental Fig. 1). The scrambled control group mice consistently performed approximately 80% correctly from day two. On the other hand, the

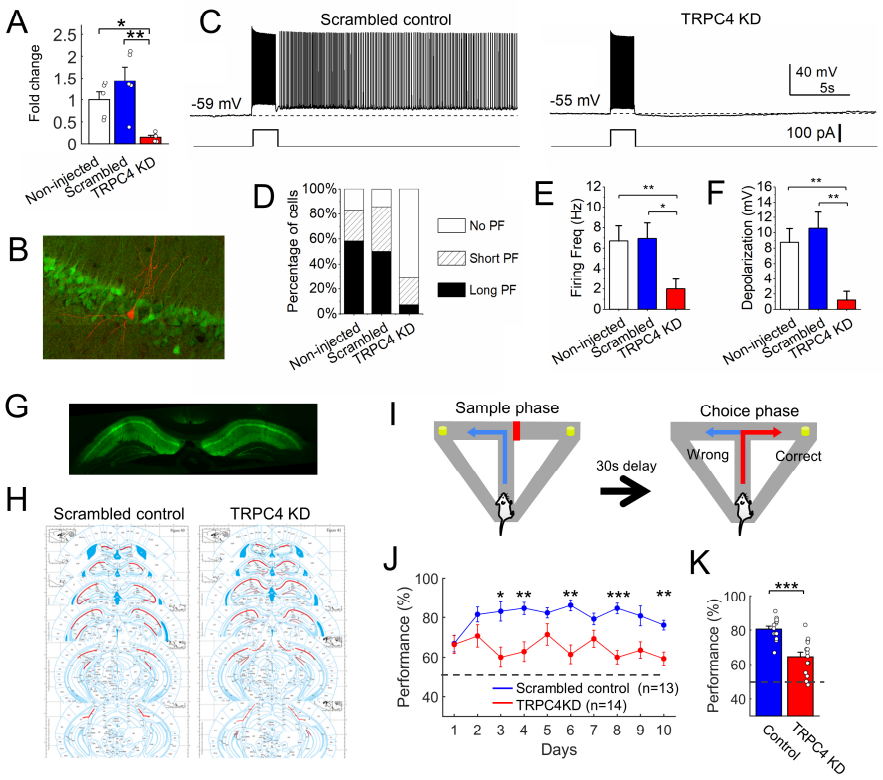

Figure 1. Hippocampal TRPC4 KD significantly reduces intrinsic persistent firing and impairs the delayed non-match-to-sample spatial working memory task (A) Reduced TRPC4 mRNA expression by the TRPC4 KD virus confirmed by RTq-PCR (one-way ANOVA, $p < 0.01$; Tukey post-hoc test corrected for multiple comparison, No virus vs Scrambled: $p = 0.33$, No virus vs TRPC4 KD: $p < 0.05$, Scrambled vs TRPC4 KD: $p < 0.01$; $n = 5$ in all groups). (B) An example hippocampal slice with GFP-expressing cells due to TRPC4 KD virus injection and a recorded neuron (red). (C) Persistent firing observed in a CA1 pyramidal cell infected with the scramble control virus (upper trace) and an absence of persistent firing in a cell infected with the TRPC4 KD virus (lower trace). The bottom trace indicates injected current. The red part of this trace corresponds to the 10 s interval when firing rate and depolarization were measured in E and F. (D) Percentages of cells responded with persistent firing ($n = 12$, 14 and 14, respectively; No PF: no persistent firing. Short PF: persistent firing which did not last for 30 s. Long PF: persistent firing lasted longer than 30 s). Fisher's exact test, Non-injected vs Scrambled: $p = 1$; Non-injected vs TRPC4 KD: $p = 0.0079$; Scrambled vs TRPC4 KD: $p = 0.0063$. (E and F) TRPC4 KD significantly decreased frequency of persistent firing and membrane depolarization measured during the 10 s period after the triggering stimulus (Frequency: Kruskal Wallis test, $p = 0.0023$, Chi-sq = 12.18, df = 2; Tukey post-hoc test, Non-injected vs Scrambled: $p = 0.99$, Non-injected vs TRPC4 KD: $p = 0.0077$, Scrambled vs TRPC4 KD: $p = 0.0074$; Depolarization: Kruskal–Wallis test, $p = 0.0116$, Chi-sq = 8.92, df = 2; Tukey post-hoc test, Non-injected vs Scrambled: $p = 0.89$, Non-injected vs TRPC4 KD: $p = 0.017$, Scrambled vs TRPC4 KD: $p = 0.047$; $n = 12$, 14 and 14, respectively). KD, knockdown; ANOVA, analysis of variance. (G) An example of hippocampal GFP expression after TRPC4 KD virus injection. (H) Summary of virus expression along the rostro-caudal axis from all mice. Red lines indicate the maximum extent of virus spread in each rostro-caudal plane. (I) The delayed non-match-to-sample spatial working memory task in a T-maze. (J) Working memory performance in scrambled control and TRPC4 KD group animals over ten days. Two-way ANOVA suggested significant main effects of the animal group ($p < 0.0001$). T-tests corrected for multiple comparisons suggested significant differences on days 3 ($p = 0.020$), 4 ($p = 0.0086$), 6 ($p = 0.0019$), 8 ($p < 0.001$), and 10 ($p = 0.0040$). (K) Averaged working memory performances of TRPC4 KD mice were significantly lower than the scrambled control group (T-test, $p < 0.001$; $n = 13$ and 14, respectively). KD, knockdown; ANOVA, analysis of variance.

performance of the TRPC4 KD group remained approximately 60% correct over the ten days of testing (Fig. 1J). Group comparisons demonstrated that hippocampal TRPC4 KD significantly impaired working memory performance compared to scrambled control mice (Fig. 1K). These results indicate that TRPC4 channels in CA1 neurons are necessary for spatial working memory.

TRPC4 KD suppresses *in vivo* persistent firing

Classical theory and evidence suggest that persistent firing supports memory maintenance[8,33,42]. We tested whether TRPC4 KD affected persistent firing in the T-maze using *in vivo* recordings. We observed cells with increasing firing rates during the delay (maintenance) period (0–30 s; orange line, Fig. 2A). To quantify such increased firing, we calculated the z-scored firing rate of individual cells around the delay period using the pre-delay period as the baseline in cells from the control and TRPC4 KD groups (Fig. 2B, see Methods). The cells were sorted based on their mean activity during the delay period (0–25 s; orange line at the top of Fig. 2B). While a substantial portion of cells at the top of the figure showed increased activity during the delay in the control group (top ~10%; Fig. 2B, left), such an increase was less prominent in the TRPC4 KD group (Fig. 2B, right). The activity of the top 10% cells was significantly lower in the TRPC4 KD group (top panels in Fig. 2C and D). Similarly, suppression of the bottom 10% cells in the TRPC4 KD group was significantly weaker (bottom panels in Fig. 2C and D), indicating that both positive and negative modulations were compromised in the KD group. Accordingly, TRPC4 KD significantly reduced the number of delay-activated (Act) and delay-suppressed (Sup) cells and increased the number of non-modulated (NM) cells (Fig. 2E).

If intrinsic persistent firing was supporting *in vivo* persistent firing, TRPC4 KD should increase transiently active cells. To test this, we sorted the cells using only activity during the first two seconds of the delay period (0–2 s, Fig. 2F). The activity of initially active cells significantly decreased during the delay period in the KD group, whereas more cells in the control group maintained their activity until the end of the delay period (Fig. 2F and G). The activity measured during the entire delay period (0–25 s) was significantly lower in the KD group (Fig. 2H). We measured the temporal field duration to quantify the duration of continuous elevation of the firing rate (Fig. 2I; see Methods). While the control group showed a wide distribution of temporal field duration up to the full delay duration, the majority

153 of the TRPC4 KD group cells showed a temporal field shorter than 7.5 s (Fig. 2I, upper panel). The

154 mean temporal field duration was significantly shorter in the TRPC4 KD group (Fig. 2I, lower panel).

155 These data indicated that TRPC4 KD increased transient firing *in vivo,* as expected from our *in vitro*

156 results.

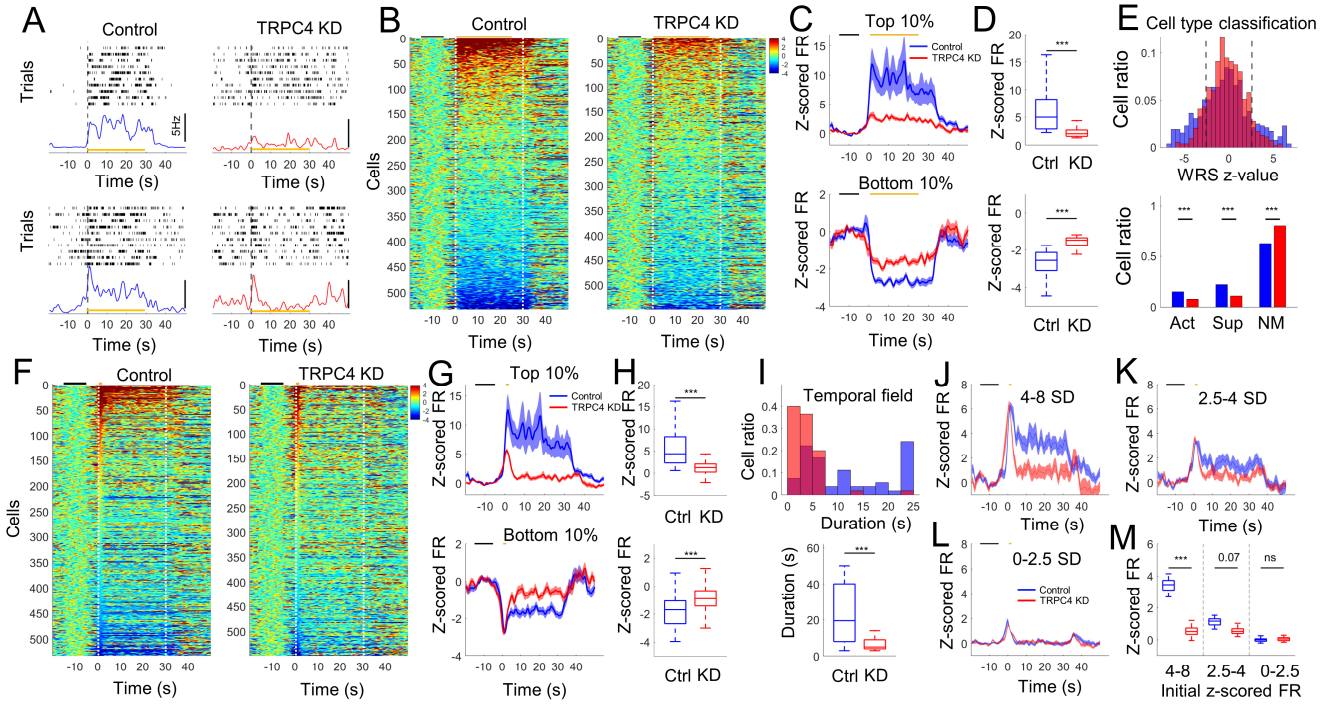

Figure 2. TRPC4 KD suppresses in vivo persistent activity (A) Example firing pattern (raster plot) and averaged firing rate (lower panel) of two cells from the control and TRPC4 KD groups around the delay period of the spatial working memory task. (B) Z-scored firing rate of all cells sorted by the delay period activity. Vertical dashed lines indicate the onset and offset of the delay period. Black and orange horizontal lines at the top of each panel indicate the baseline period and period for cell sorting, respectively. (C) Averaged z-scored firing rate (FR) of the top (upper panel) and bottom (lower panel) 10% cells in B. (D) Comparison of z-scored firing rate of the top (upper panel) and bottom (lower panel) 10 % cells in B averaged over the delay period (0–25 s) (WRS test, $p < 0.001$ and $p < 0.001$ for upper and lower panels respectively). (E) Classification of activated (Act), suppressed (Sup), and non-modulated (NM) cells using the Wilcoxon rank sum (WRS) test. The upper panel shows the distribution of WRS z-values, and the lower panel shows the ratio of cells in each category (Chi-square test, $p<0.001$ for all categories). (F) Z-scored firing rate of all cells sorted by the activity at the initial part of the delay period (0–2 s). Black and orange horizontal lines at the top of each panel indicate the baseline period and period for cell sorting, respectively. (G) Averaged z-scored firing rate of top (upper panel) and bottom (lower panel) 10% cells in F. (H) Comparison of z-scored firing rate of the top (upper panel) and bottom (lower panel) 10% cells in F averaged over the delay period (0–25 s) (WRS test, $p < 0.001$ and $p < 0.001$ for upper and lower panels respectively). (I) Distribution (upper panel) and comparison (lower panel) of temporal field duration among the top 10% cells (WRS test, $p < 0.001$). (J-L) Averaged z-scored firing rate of cells that showed 4-8 (J), 2.5-4 (K), and 0-2.5 (L) SD peak z-scored firing rate at the initial part of the delay (0-2 s). (M) Comparison of activity during the delay (4-25 s) period in cells that showed different levels of initial activation corresponding to J to L (WRS test, $p < 0.001$, $p = 0.07$, and $p = 0.58$ for J, K, and L, respectively). KD, knockdown

157 However, the initial activity of the top 10% cells was stronger in the control group (Fig. 2G,
158 upper panel), which could have resulted in stronger persistent firing in this group. To test this possibility,
159 we filtered cells based on their initial (0-2 s) activity levels (Fig. 2J-M). The control group cells with
160 initial activity increases of 4–8 and 2.5–4 standard deviations (SD) maintained a greater elevated level
161 of activity until the end of delay compared to KD group cells (Fig. 2J and K), whereas those with initial
162 activity of 0–2.5 SD did not show elevated activity (Fig. 2L). The sustained activity measured at 4–25
163 s was smaller in the KD group with 4–8 and 2.5–4 initial SD (Fig. 2M), indicating that the different
164 activities between the two groups are not simply due to the difference in initial activation. Thus, more
165 KD cells showed transient activity during the delay period, supporting the contribution of TRPC4
166 channels to sustained activity *in vivo* in a similar manner as *in vitro*.

167 **Temporal sorting reveals reduced persistent firing in TRPC4 KD mice**

168 We further characterized the effect of TRPC4 KD using temporal sorting[11,12]. For this analysis, we
169 selected putative pyramidal cells active (firing rate > 2 Hz) in at least one bin during or near the delay
170 period (see Methods, 196/533 control cells and 235/549 TRPC4 KD cells) and sorted them according
171 to their activity peak time, as in previous reports[11] (Fig. 3A). We found an overrepresentation of the
172 initial part of the delay period (0–3 s) in both the control and TRPC4 KD group (Fig. 3B). However,
173 TRPC4 KD did not significantly alter peak time distribution.

174 To evaluate potential effects of TRPC4 KD on cells with different peak times, cells were
175 separated into three groups based on their peak times during the delay (Fig. 3A). While cells that peaked
176 at 0–2.5 s (group 1) showed transient peak activity, the other two groups that peaked later in the delay
177 (2.5–16.5 s: group 2, 16.5–30 s: group 3) exhibited, on average, an elevated firing rate throughout the
178 delay period in the control group (Fig. 3C left). While TRPC4 KD did not affect the transient activation
179 of cells at the initial part of the delay (group 1), it reduced long-lasting elevated firing of group 2 and 3
180 cells (Fig. 3C, right). Accordingly, the firing rate averaged over the delay period was significantly lower
181 in groups 2 and 3 of the KD group but not in group 1 (Fig. 3D). Combining all cells that peaked during
182 the delay, the KD group had more cells with shorter fields (See Methods; Fig. 3E). The duration of the
183 field from the KD group cells was significantly shorter in groups 2 and 3 (Fig. 3F). The specific effect

184 of TRPC4 KD on cells with longer temporal fields, further support the idea that the ability of single

185 neurons to sustain firing is necessary specifically for persistent firing *in vivo*.

186

187 **Activity outside the delay period is intact**

188 To further assess whether the effect of TRPC4 KD was specific to the delay period, we compared the

189 activity of cells at different time points, ranging from 4 s before delay onset to 3 s after the delay (Fig.

190 4). First, cells were sorted using the z-scored activity of each cell at 3 to 4 s before the start of the delay

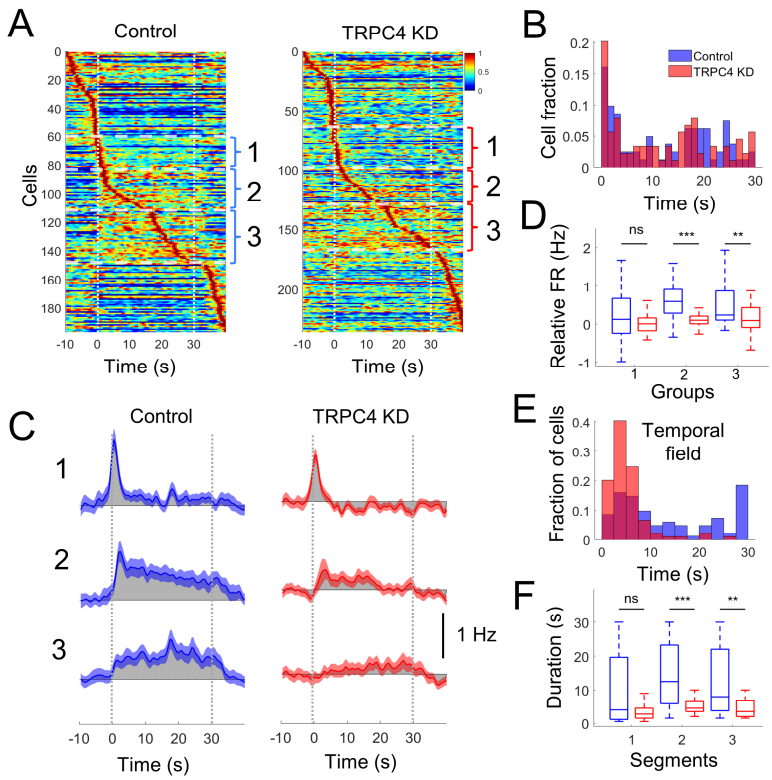

Figure. 3. Peak time sorting also shows reduced persistent activity in TRPC4 KD mice
(A) Normalized firing rate of cells sorted by their peak times. Vertical dashed lines indicate the onset and offset of the delay period. Horizontal dashed lines and numbers (1-3) on the right of each panel indicate divisions of cells by their peak times (group 1: 0–2.5 s, group 2: 2.5–16.5 s, and group 3: 16.5–30 s). (B) Distribution of peak time of all cells within the delay period. Peak time distribution is not significantly affected by TRPC4 KD (WRS test, $p = 0.74$). (C) Averaged relative firing rate (compared to baseline firing rate) of cells belonging to each peak time segment shown in A. Gray shades indicate a difference from the baseline firing rate. Note, a prominent, long-lasting elevated firing rate in control cells in groups 2 and 3. (D) Relative firing rate (FR) measured during the delay (0 to 30 s) compared to the baseline period in cells in each peak time segment. (E) Distribution of temporal field duration of all cells peaked during the delay period (group 1-3) (WRS test, $p < 0.001$). (F) Comparison of the duration of the field in each group (WRS test, $p = 0.32$, $p < 0.001$, and $p = 0.006$ for groups 1, 2, and 3, respectively). KD, knockdown

period (-4 to -3 s; Fig. 4A), and the average activity of the top 10% cells from the control and KD groups was compared (Fig. 4D most left). These cells were only temporarily active and did not display persistent firing in either group, indicating that persistent firing was not ubiquitous. Neither activity of

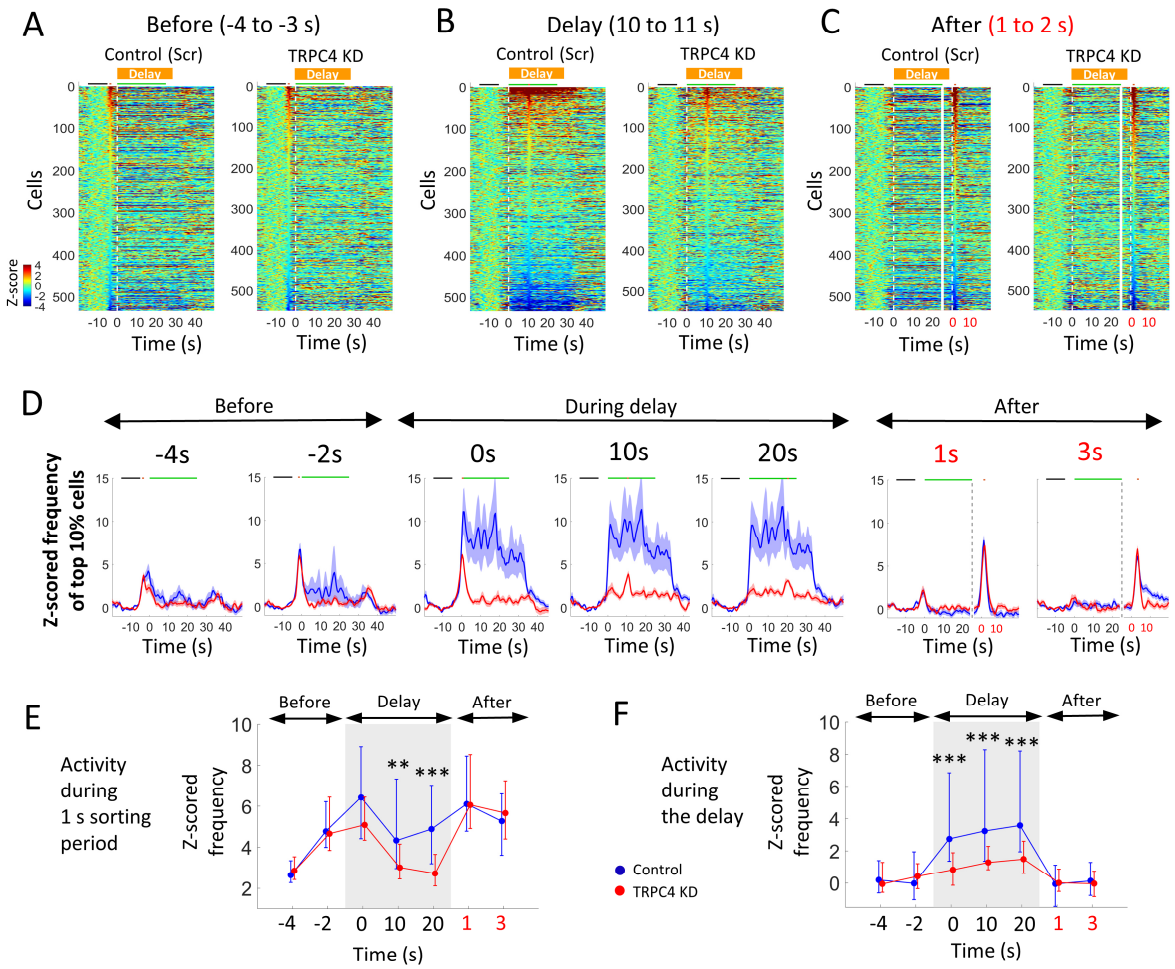

Figure 4. Activity outside the delay period is not strongly affected by TRPC4 KD (A-C) Z-scored firing rate of all cells sorted by their activity during the (A) 4 to 3 s before delay, (B) 10 to 11 s from the start of delay, and (C) 1 to 2 s after the delay offset. Vertical dashed lines indicate the onset and offset of the delay period. Black, orange, and green horizontal lines at the top of each panel indicate the baseline period, period for cell sorting, and period for delay activity measurement, respectively. In C, the white solid vertical line indicates the separation of the color plot into two parts that are aligned to the delay onset (left of the line) and offset (right of the line). (D) Averaged z-scored firing rate of the top 10% cells at different time points. Note that the cells chosen for each panel are therefore different. The vertical dotted lines in the two last panels correspond to the time when data alignment changed as in C. (E) Comparison of z-scored firing rate of the top 10 % cells measured specifically during the one second-long sorting period (corresponding to the orange horizontal lines in D; Ranksum test with Bonferroni correction, p = 0.31, 1.45, 0.29, 0.003, < 0.001, 1.45, 0.28, respectively). (F) Comparison of z-scored firing rate of the top 10 % cells measured specifically during the delay period (corresponding to the green horizontal lines in D; Ranksum test with Bonferroni correction, p = 0.88, 1.46, < 0.001, < 0.001, < 0.001, 1.47, 1.10, respectively). Data points show the median, and error bars indicate the upper and lower quartiles. KD, knockdown

194 the top 10 % cells during this 1 s window (-4 s in Fig. 4E) nor during the entire delay period (-4 s in
195 Fig. 4F) differed between the control and KD groups, indicating that TRPC4 KD did not have a strong
196 effect before the delay. Similar results were obtained 2 s before delay onset (-2 to -1 s; Fig. 4D, second
197 from left; Time -2 s in Fig. 4E and F). In contrast, control group cells activated during the delay (0-1,
198 10-11 and 20-21 s) showed stronger activity than KD cells, both during these 1s windows and during
199 the entire delay (Fig. 4B; Fig. 4D middle three panels; Time 0, 10, and 20 s in Fig. 4E and F). Finally,
200 when active cells were detected after the delay period (1-2 and 3-4 s later; Fig. 4C; Fig. 4D, two
201 rightmost panels), the activity of these cells was transient and similar between the two groups (Time 1
202 and 3 s in Fig. 4E and F). This suggests that persistent firing does not occur before or after the delay
203 period, and that TRPC4 KD specifically affects the activity of neurons during the delay period, as
204 opposed to worsening the signal-to-noise ratio throughout the task.
205
206 **Activity of putative pyramidal cells and interneurons**
207 We next investigated whether the difference in the delay period activity between control and TRPC4
208 KD mice was cell type-dependent. We separated recorded neurons into putative pyramidal neurons and
209 interneurons based on their average firing rates and spike durations (see Methods). Putative pyramidal
210 cells in the control group showed strong activity during the delay, with TRPC4 KD suppressing this
211 activity (Supplemental Fig. 2A-D). On the other hand, the activity of the top 10% putative interneurons
212 during the delay period did not differ between the control and TRPC4 KD groups (Supplemental Fig.
213 2E-H). This suggests that putative interneurons are not the main source of the observed TRPC4 KD-
214 dependent changes.
215
216 **Information coded by persistent firing**
217 Next, we investigated the nature of information coded by cells with strong persistent firing during the
218 delay period. The hippocampus may support spatial working memory in at least two ways. First,
219 persistent firing may sustain working memory content (e.g., turn direction in the sample trial) during
220 the delay period[33,42]. Second, the hippocampus may support spatial working memory tasks by providing

221 information of the current spatial location[34,43]. However, whether the long-lasting persistent firing codes

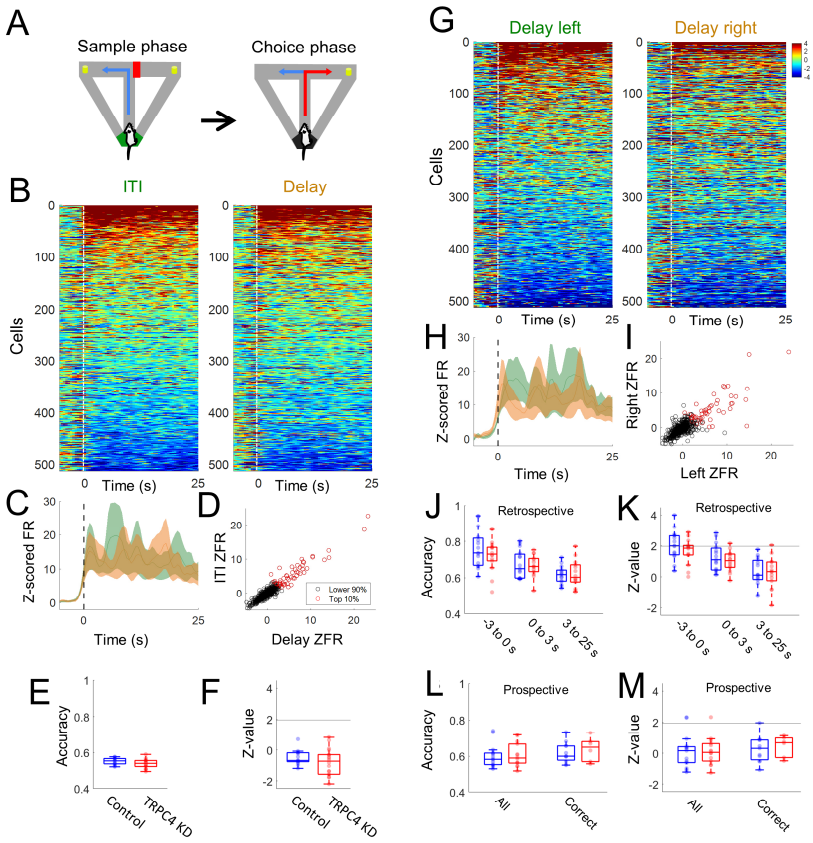

Figure 5. Persistently firing cells do not strongly code task phases and direction of turn (A) Inter-trial-interval (ITI, green) in the sample phase and delay period (orange) in the choice phase. Animals were in the same start box in the ITI and delay period. (B) Z-scored firing rate of all cells sorted by the averaged activity during the ITI (0–25 s) in both ITI and delay. Vertical dashed lines indicate the onset of ITI or the delay period. Baseline and sorting period were the same as in Fig. 2B. (C) Averaged activity of the top 10% cells in B from ITI (green) and delay period (orange; WRS test, p = 0.40). (D) Comparison of activity during ITI and the delay period from all cells. Each circle corresponds to a cell. The top 10% cells (based on common sorting) are indicated by red circles. (E-F) Accuracy (E) and z-value (F) from the SVM prediction of ITI vs delay phase based on the activity of all cells (WRS test, p = 0.61 and p = 0.59 for E and F, respectively). The horizontal line in F indicates a 5% significance level. (G) Z-scored firing rate of all cells near the delay period, sorted by the average activity of the left trials. Here, the left and right trials are defined by the direction of the turn at the sample phase (retrospective coding). (H) Averaged activity of the top 10 % cells in G from the left (green) and right (orange) trials. (WRS test, p = 0.0058). (I) Comparison of activity from left and right trials for all cells. Each circle corresponds to a cell. The top 10% cells (based on common sorting) are indicated by the red circles. (J-K) Accuracy (J) and z-value (K) from the SVM prediction of left vs right trials based on the activity of all cells at different segments before (-3 to 0) and during (0 to 3s, 3 to 25 s) the delay period (WRS test, p = 0.49, 0.91 and 1 in J; p = 0.20, 0.28 and 0.98 in K). (L-M) Accuracy (L) and z-value (M) from the SVM prediction of future left vs right trials based on the activity of all cells during (3 to 25 s) the delay period (prospective coding). This analysis was done using all (correct and wrong) and only correct trials (WRS test, p = 0.98 and p = 0.59, respectively, in L; WRS test, p = 0.78 and p = 0.52, respectively, in M). SVM, support vector machine

222 for the turn direction or current spatial information remains unclear.

223 We first compared the activity of cells in the control group during the delay period with that
224 during the inter-trial interval (ITI; Fig. 5A). Since the animals were in the same start area in both the
225 delay period and ITI, the different activities in these phases may suggest the coding of task-relevant
226 information. Cells were sorted according to their activity during the delay period (Fig. 5B). Control
227 cells highly active during the delay period were strongly active during ITI as well, without significant
228 difference, as shown in Fig. 5B and C. The activity of individual cells during the delay period was
229 similar to that during ITI, as shown in Fig. 5D.

230 We further used a support vector machine (SVM) to test whether it could be trained to predict
231 the delay and ITI phases based on the activity of all cells in each recording session (control: n = 16,
232 TRPC4 KD: n = 18 sessions; see Methods for details; Fig. 5E and F). SVM could not differentiate the
233 delay vs. ITI phases in any of the recordings (Z-values were lower than 1.96) from the control and
234 TRPC KD groups. Furthermore, there were no differences between the control and KD groups.
235 Together, these findings contradicted the idea that persistent firing codes for task-phase-relevant
236 information.

237 Second, we asked whether the direction of the past or future turns was coded in persistent
238 activity observed during the delay period. We sorted cells from the control group using the delay activity
239 of the left trials (left turn on the sample trial; Fig. 5G, left) and used the same order for the delay activity
240 of the right trials (Fig. 5G, right). A small but significant difference was observed when comparing the
241 activity of the top 10% cells (Fig. 5H). The activity of individual cells in the left and right delay periods
242 was generally similar but showed more differences than the comparison between the ITI and delay
243 phases (Fig. 5I). While this difference between the left and right delay activity indicates the potential
244 existence of coding of the turn direction, random noise may result in such differences.

245 Therefore, we further used an SVM to test whether the population activity codes for the left vs.
246 right turn in each recording session (control, n = 15; TRPC4 KD, n = 14). SVM prediction accuracy
247 exceeded 70% in most of the sessions (Fig. 5J) just before the onset of the delay period (-3 to 0 s), when
248 the animal was still in the return arm of the T-maze, and this prediction accuracy was significantly
249 higher than the chance level in approximately half (53.3%) of the sessions (Fig. 5K). However,

250 prediction performance decreased quickly as the delay started (0–3 s; Fig. 5J and K), and almost none
251 of the sessions reached a significant level in either the control or TRPC KD group after 3 s (3–25 s) in
252 the delay period. No difference was observed between the SVM performance of the control and KD
253 groups for any of the three time-segments.

254 We further asked whether the delay period activity codes for the future turn direction
255 (prospective coding) rather than the past turn direction from the sample phase (retrospective coding).
256 The SVM prediction for prospective coding was tested using the activity from the 3-25 s period during
257 the delay of all or only correct trials (Fig. 5L and M). Most of the session did not reach significant levels
258 both in the control and KD group and there was no difference between the control and KD. Together,
259 these suggest that coding for the direction of turns during the delay period is weak. These agree with
260 recent publications which pointed out that hippocampal delay period activity does not[35,44] or only
261 weakly[45] codes for the direction of the past or future turns.

262

263 **Persistently active cells encode spatial information**

264 Next, we tested the hypothesis that persistently active cells primarily code for spatial information.
265 Computational models of hippocampal place cells suggest that spatial representation is maintained by
266 the self-sustained activity of a subset of place cells[40]; therefore, persistent firing might be involved in
267 the maintenance of spatial representation. We first sorted cells in order of the strength of persistent
268 firing during the delay period as in the previous sections (Fig. 6A). We then calculated the spatial
269 information of each cell using the entire duration of the recording, including the sample and choice
270 phases from all 10 trials (Fig. 6B). Spatial information was particularly high in the control group cells
271 which showed strong persistent firing (blue line, Fig. 6B). Spatial information of the top 10% cells in
272 Fig. 6A was significantly lower in the KD group compared to the control group (Fig. 6C), whereas that
273 of the bottom 10% cells was significantly higher in the KD group (Fig. 6D).

274 We visualized the spatial rate maps of the top 10% cells in control and TRPC4 KD groups (Fig.
275 6E and F). While the control group cells generally showed a clear field within the start area, fields of
276 TRPC4 KD cells were less confined, often having multiple fields outside the start area (Fig. 6E and F).

The averaged rate map from top 10% control cells showed a distinct firing at the start area, while that from the KD cells showed spatially less defined activity (Fig. 6G and H). This suggests that cells with

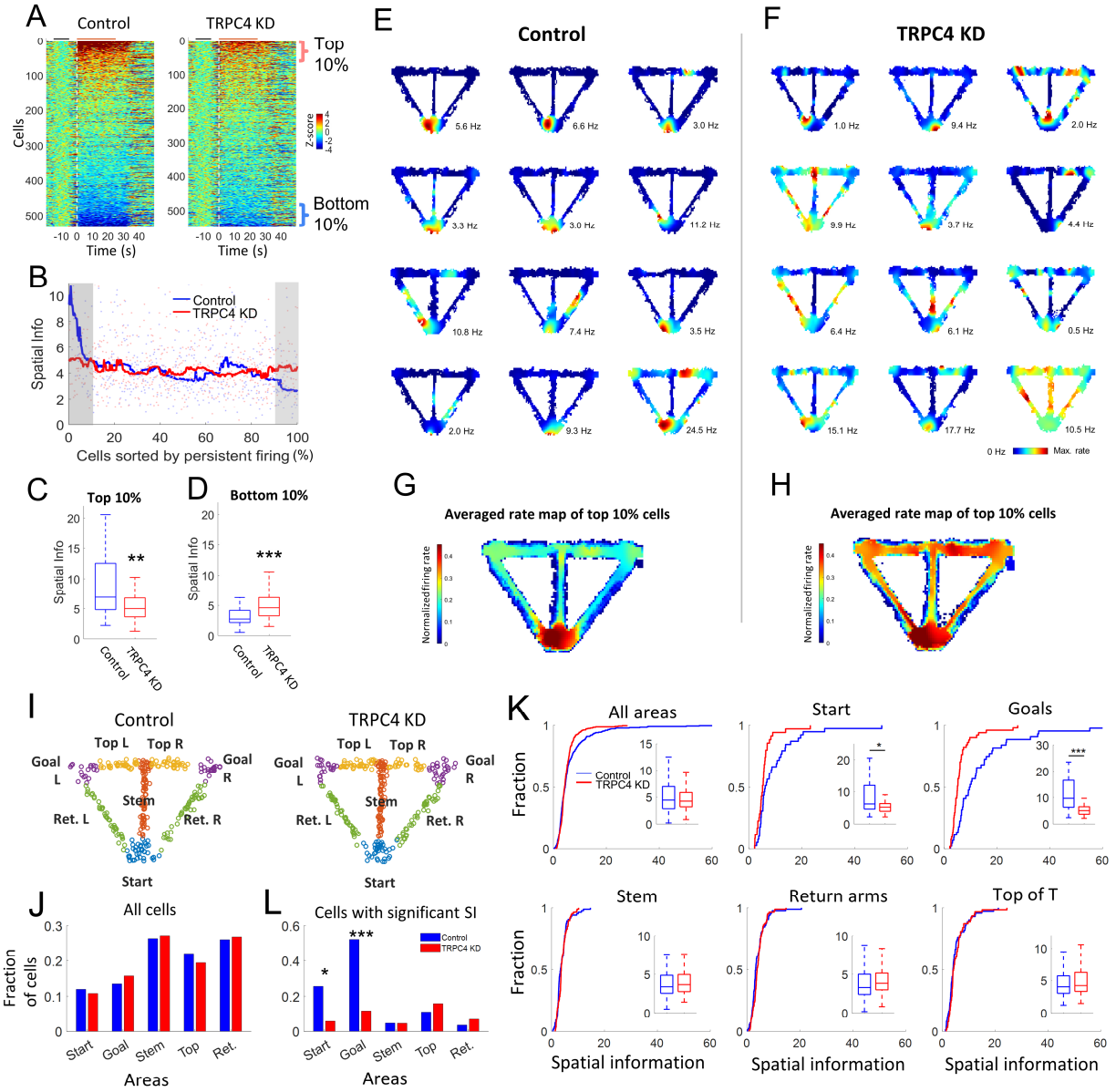

Figure 6. TRPC4 supports persistent activity of spatial cells when animals stay in a place for an extended duration (A) Z-scored firing rate of all cells sorted by the averaged activity during the delay period (0–25 s), as in Fig. 2B. Vertical dashed lines indicate the onset of the delay period. (B) Spatial information of all cells plotted in the order of the sorting in A. Solid lines indicate the moving average. Red and blue shaded areas indicate the top and bottom 10% cells. (C and D) Comparison of spatial information between the control and TRPC4 KD groups in the top (C; WRS test, $p = 0.0024$; $n = 53$) and bottom (D; WRS test, $p < 0.001$; $n = 55$) 10% cells. (E and F) Example spatial rate maps of the top 10% cells in control (E) and TRPC4 KD (F) groups. The maximum firing rate of each cell is indicated at the bottom right corner of each panel. (G and H) Averaged spatial rate maps of all top 10 % cells in the control (G) and TRPC4 KD (F) groups. (I) Distribution of peak firing location of all putative pyramidal cells on the T-maze. Each circle corresponds to a cell, and colors indicate different sub-areas. Top: top of the T-maze, Ret.: return arm, L: Left, R: Right. (J) Fractions of cells classified into each sub-area. (K) Distribution of spatial information of cells in all and each sub-area. Insets are comparisons of spatial information between the control and KD cells (WRS test, All areas: $p = 0.56$, Start: $p < 0.019$, Goals: $p < 0.001$, Stem: $p = 0.41$, Return arms: $p = 0.19$, and Top of T: 0.35). (L) Number of place cells with significant spatial information in each sub-area (Fisher's exact test, $p = 0.027$, < 0.001, 1, 0.45, and 0.49, respectively, from left to right). KD, knockdown

279 strong persistent firing during the delay period are those with better-defined place fields in the start area
280 and consequently have higher spatial information. This suggests that TRPC4 KD destabilized spatial
281 representation by preventing persistent activity of CA1 place cells while the animal remained in the
282 start area.
283
284 **Selective decrease of spatial information in start and goal areas**
285 In the T-maze task, in addition to the start area, the animals stayed for an extended period in the goal
286 areas where they consumed their rewards, whereas they run through other subareas of the maze (e.g.,
287 stem, return arm). If intrinsic persistent firing supports continuous place cell activity, TRPC4 KD might
288 have affected spatial representation specifically in the start and goal areas without affecting that in other
289 subareas. To test this, we first detected the location of firing fields within the T-maze for each putative
290 pyramidal cell (see Methods). Next, we divided cells into different groups depending on the subareas
291 of the T-maze where the location of field centers fell (Fig. 6I). The number of cells in each subarea was
292 similar in the control and KD groups (Fig. 6J).
293 We then compared the spatial information of the cells in each subarea (Fig. 6K). Spatial
294 information was slightly smaller in the TRPC4 KD group when all subareas were combined (all areas),
295 without a significant difference. Consistent with previous observations, the spatial information of the
296 cells in the start area was significantly lower in the KD group. Interestingly, a similar difference was
297 observed in the goal area, where the animals stayed for an extended time. However, spatial information
298 was not significantly different in other areas, such as the stem, return arms, and top of the T. Moreover,
299 the number of place cells (cells significantly modulated by location) was higher in the control group
300 than in the KD group only in the start and goal areas (Fig. 6L). These results suggest that TRPC4 KD
301 selectively impairs the spatial representation when animals stay in a place, and place cells need to fire
302 persistently. These suggest that TRPC4 KD specifically affects the maintenance of spatial
303 representation when animal remained at the same place.
304 Additional analyses indicated that the compromised spatial representation observed in the start
305 and goal areas in the TRPC4 KD animals is not associated with a lower running speed or weaker theta
306 oscillations (Supplemental Fig. 3). These spatial analyses are in line with the time-domain analysis (Fig.

307 4), which revealed a specific effect of TRPC4 KD on cellular activity during, but not before or after,
308 the delay.
309
310 **Gradual decrease of left and right goal representation**
311 We further analyzed cellular activity and spatial representation in the goal areas (Fig. 7) since the
312 encoding of left vs. right goals in the hippocampus during the sample phase may be crucial for task
313 performance[43]. First, we tested whether persistent activity differed in the goal areas. We limited our
314 analysis to trials in which animals spent at least 10 s continuously within the goal area (see Methods for
315 details). Fig. 7A shows the z-scored firing rate of all cells where the time 0–10 s corresponds to the 10
316 s period when animals continuously stayed in the left goal area in the sample phases (indicated by the
317 orange line on the top). Activity of the top 10% cells was significantly lower in the TRPC4 KD group,
318 both in the left and right goals (Fig. 7B and C). These results indicated that TRPC4 KD reduced the
319 continuous activity of cells in the goal area as in the start area.
320 Next, we investigated whether this affected the representations of the left and right goals at the
321 population level using an SVM (Fig. 7D and E). This analysis was conducted using the activity of all
322 cells from the 10 s goal period in each recording session with a minimum of 15 cells (n = 15 and 14
323 sessions in the control and KD groups, respectively). The left vs. right goal prediction accuracy and z-
324 values of the SVM analysis were significantly lower in the TRPC4 KD group (Fig. 7D and E). While
325 80.0% of sessions had significantly higher prediction accuracy than chance level in control, only 42.8%
326 were significantly higher than chance level in the KD group (Fig. 7E), suggesting that representations
327 of left vs. right goals may have been compromised in the TRPC4 KD group.
328 We further investigated whether a gradual decline in left and right goal representation may be
329 detected over time within the 10 s goal period owing to the lack of persistent activity in the TRPC4 KD
330 group (Fig. 7F and G). We performed a similar SVM analysis at different time points starting from the
331 pre-goal period (-3.5 s) using a sliding (1 s) 5 s window (time indicated in Fig. 7F and G is the center
332 of the window). The prediction accuracy increased over time as the animal approached the goal area (-
333 3.5 to +1.5 s, note that +1.5 still includes 3 s of pre-goal time). Importantly, the prediction accuracy and

z-value between the control and KD groups differed starting at +4.5 s into the goal area (Fig. 7F and G), indicating a faster decline in goal representation in the KD group.

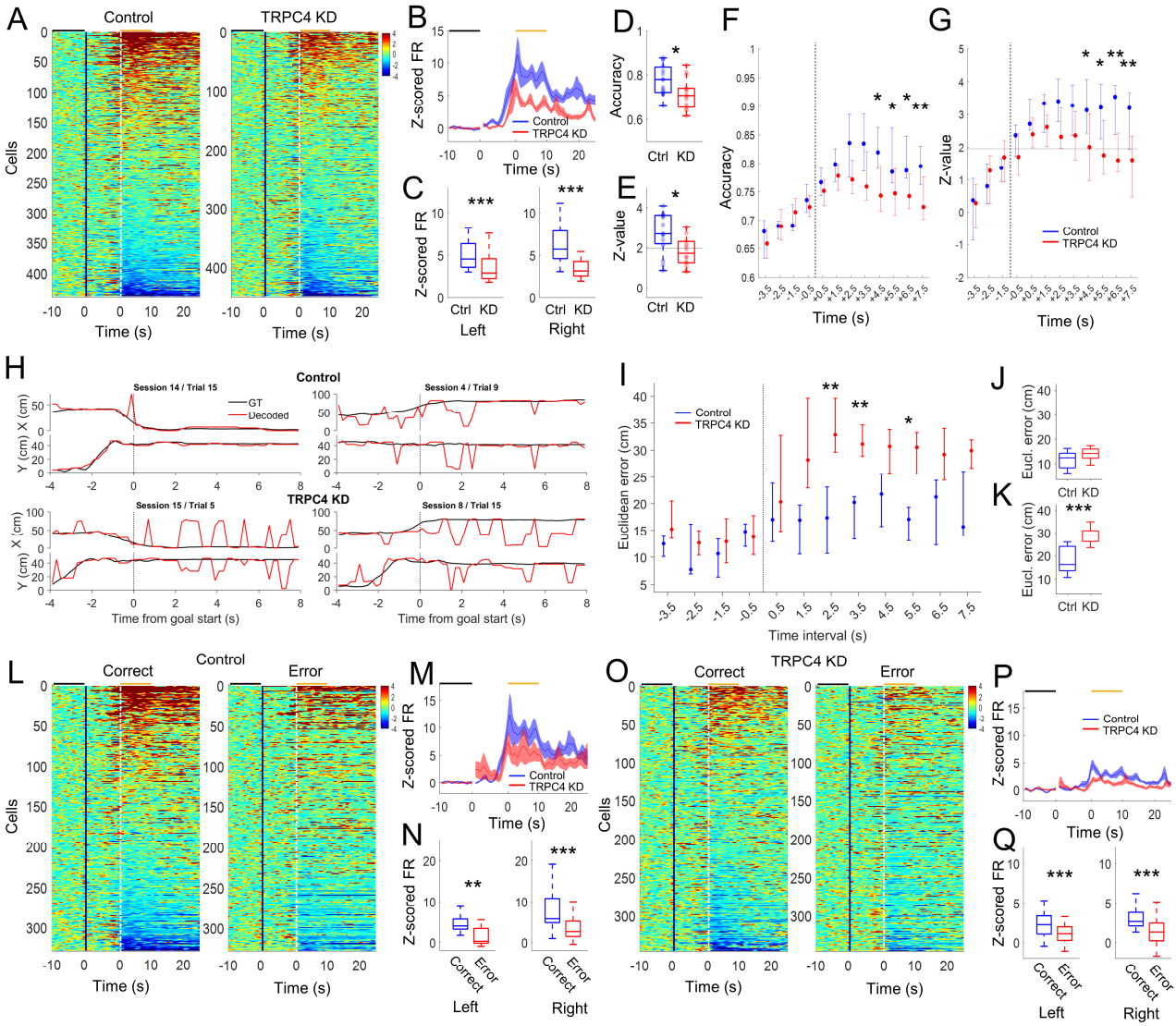

Figure 7. Gradual decrease of spatial representation in the goal areas may have resulted in the poor task performance of TRPC4 KD mice (A) Z-scored firing rate of cells sorted by their activity during the 10 s goal period when animals continuously stayed in the left goal area. The black vertical gap separates the first 10 s, which is referenced to the end of the ITI period, and the rest, which is referenced to the start of the goal entry. The black and orange horizontal lines on the top indicate the baseline and 10 s goal period, respectively. (B) Activity of the top 10% cells in A. (C) Comparisons of activity of the top 10% cells during the 10 s goal period (0-10 s) at the left and right goals (WRS test, $p < 0.001$ and $p < 0.001$, respectively). (D-E) Accuracy (D) and z-value (E) from the SVM prediction of left vs right goals based on the activity of all cells in individual sessions during the 10 s goal period (WRS test, $p = 0.019$ and 0.017 in D and E, respectively). The horizontal line in E indicates a 5% significance level. (F-G) Accuracy (F) and z-value (G) from the SVM prediction of left vs right goals at different time periods before and during the 10 s goal period. The vertical dotted lines indicate goal entry, and the horizontal line in G indicates 5% significance level. (H) Example real (GT) and decoded X and Y positions of mice from 4 s before to 8 s after goal entry. Dashed lines indicate time of goal entry. (I) Decoding error measured as distance between true and estimated positions at different time periods before and during the goal period. (J and K) Comparison of error distance between the control and the KD groups before (-4 to 0 s) and after (0 to 8 s) goal entry (WRS test, $p = 0.19$ and 0.001, respectively). *(legend continue to next page)*

(L) Z-scored firing rate of cells from the control group animals sorted by their combined sort order (see text) during the 10 s goal period in the left goal area from the correct (left panel) and error (right panel) trials. (M) Activity of the top 10% cells in L. (N) Comparisons of activity of the top 10% cells during the 10 s goal period (0-10 s) from correct (blue) and error (red) trials at the left and right goals (WRS test, $p = 0.0018$ and < 0.001, respectively). (O-Q) Same as panels L to N but for the TRPC4 KD group (WRS test, $p < 0.001$ and < 0.001, for left and right trials, respectively in Q). Ctr, control; KD, knockdown.

To test more directly the effect of TRPC4 KD on hippocampal spatial representations at the goal areas, we used Bayesian decoding of animal's position based on the population activity (see Methods). In each trial, the actual position of the mouse (black trace) was compared with the decoded position (red trace) from 4 s before goal entry, when mice were in the stem and top of the T parts of the T-maze, until 8 s after the goal entry (Fig. 7H). While the position estimation was in general good in both control and TRPC4 KD group mice before the entry to the goal area, estimation errors increased in the TRPC4 KD group after the entry to the goal area (Fig. 7I). The estimation error between control and KD mice was not different before the entry to the goal area (-4 to 0 s; Fig. 7J) but was significantly larger in the KD group after the entry (0 to 8 s; Fig. 7K). This is in line with the data in the previous section where the spatial information was not different in the stem and the top of the T parts but was smaller in TRPC4 KD group in the goal areas. Together, these suggest the specific role of TRPC4 channels on the maintenance of spatial representation.

Behavioral relevance

Finally, we asked whether the activity of the cells in the goal differed between correct and incorrect trials, using recording sessions with at least two error trials. The activity of the cells was first averaged over all trials, including both correct and error trials, to obtain combined sorting order. Subsequently, the activity profiles from correct and incorrect trials were separately averaged for each cell and sorted by the combined sort order (Fig. 7L). Persistent firing of the top 10% cells was significantly lower in the error trials compared to the correct trials in the control group for both the left and the right goals (Fig. 7M and N). Similar differences were observed in the KD group (Fig. 7O-Q). These results are consistent with the idea that hippocampal goal activity during the sample phases contributes to task performance[43,46]. Together, our data suggested that the intrinsic mechanism of persistent firing supports

359 a stable spatial representation of goal locations, which is necessary for correct encoding of left vs right
360 turns.
361

362 Discussion

363 Despite empirical evidence[19,21,24,47] and theoretical supports[26–28], it remained unclear whether individual
364 cells support persistent activity *in vivo*. We identified the TRPC4 channel as a molecular mechanism of
365 intrinsic persistent firing in CA1 pyramidal cells[25] and demonstrated that persistent firing was
366 significantly reduced *in vivo* in a spatial working memory task by TRPC4 KD (Fig. 2-3). These results
367 provide the first direct evidence that a single-cell mechanism supports persistent firing *in vivo* during a
368 cognitive task. Further analyses revealed a specific effect of TRPC4 KD on persistently firing (Fig. 4)
369 without disrupting signal-to-noise ratio in general. The behavioral outcome align with studies indicating
370 the role of TRPC channels[48,49] and manipulations that potentially disrupt persistent firing[32] in working
371 memory.

372 Classically, persistent firing during the delay period has been believed to hold working memory
373 content. Abundant evidence supports this in the prefrontal cortex and hippocampus during the working
374 memory delay period in humans and monkeys[5,8] whereas data in rodents remains mixed[35,45,50]. In
375 agreement with these rodent studies, our SVM analyses suggest the absence or very weak presence of
376 working memory content in the delay phase (Fig. 5). An alternative theory posits that the hippocampus
377 contributes to this type of working memory task by providing spatial information during the sample
378 phase to help encoding, rather than maintaining working memory content[43,51,52]. We found that neurons
379 with strong persistent firing had larger spatial information, and TRPC4 KD reduced spatial information
380 specifically in places where persistent firing was observed (start and goal areas), suggesting that
381 persistent firing mainly codes for spatial information (Fig. 6 and 7).

382 Hippocampal place cells are believed to be supported by path integration, which requires the
383 maintenance and continuous updating of spatial representation[40]. Computational studies have suggested
384 that similar attractor networks, such as continuous attractor networks, support working memory and
385 path integration[37,38]. The continuous attractor model maintains spatial representation by persistent firing

386 of a subset of neurons, “bump of activity”, through recurrent synaptic networks[38]. However, the neural
387 networks of CA1, where place cells were most intensively studied, and MEC layer II, where grid cells
388 were found, lack recurrent excitatory networks[53,54]. Additionally, these network models are sensitive to
389 distractors, whereas experimental evidence suggests their robustness to distractors[55,56].

390 Including the intrinsic cellular mechanisms of persistent firing in attractor networks has been
391 shown to ameliorate these problems increasing stability against noise, reducing drift, and reducing
392 sensitivity to parameters[28,29,57] . Upon empirically disrupting the intrinsic mechanism of persistent firing
393 *in vivo*, we observed that spatial representation was compromised specifically at the start and goal areas.
394 The intactness of spatial representation in other areas may indicate that attractor dynamics were still
395 present, in agreement with the hybrid model. The gradual degradation of goal representation in the
396 TRPC4 KD mice (Fig. 7) suggests a drift of attractor state due to the loss of persistent firing mechanism
397 in individual cells as predicted from the loss of intrinsic properties in the hybrid model[28].

398 An intact spatial representation outside the start and goal areas can be supported by external
399 cue-based navigation[58] that may not require information retention by persistent firing. Distal cues on
400 the surrounding curtains and walls were visible to animals when they were in long corridors such as the
401 stem and return arms, which was not the case in the start and goal areas. Alternatively, this could be
402 attributed to the time required for persistent firing initiation, owing to the Ca2+-dependent biochemical
403 processes involved in activating TRPC channels[20]. When the mice ran through the T-maze arms at a
404 relatively high speed, the resulting short period of activation of each place cell may not have been long
405 enough to fully activate the TRPC channels. Further studies are needed to clarify the exact mechanisms
406 TRPC4 supports spatial representation in specific areas.

407 The prevailing view that neurons fire only when they receive sufficient input dictates current
408 understanding of neural computation in the brain. Our findings challenge this view, revealing them as
409 active contributors to information retention *in vivo*. This intrinsic persistent firing depends on the
410 cholinergic system, which degrades in aging and Alzheimer’s disease[59,60] causing cognitive
411 impairments [61,62]. Our findings thus potentially reshape our general understanding of brain computation
412 and highlights novel therapeutic targets for cognitive disorders.

413

References

1. Choi, J. H. *et al.* Short-term memory errors are strongly associated with a drift in neural activity in the posterior parietal cortex. *PLoS Biol* **23**, e3003359 (2025).
2. Robinson, N. T. M. *et al.* Targeted Activation of Hippocampal Place Cells Drives Memory-Guided Spatial Behavior. *Cell* **183**, 1586-1599.e10 (2020).
3. Major, G. & Tank, D. Persistent neural activity: prevalence and mechanisms. *Curr Opin Neurobiol* **14**, 675–684 (2004).
4. Zylberberg, J. & Strowbridge, B. W. Mechanisms of Persistent Activity in Cortical Circuits: Possible Neural Substrates for Working Memory. *Annu. Rev. Neurosci.* **40**, 603–627 (2017).
5. Fuster, J. M. Unit activity in prefrontal cortex during delayed-response performance: neuronal correlates of transient memory. *J Neurophysiol* **36**, 61–78 (1973).
6. Kubota, K., Iwamoto, T. & Suzuki, H. Visuokinetic activities of primate prefrontal neurons during delayed-response performance. *J Neurophysiol* **37**, 1197–1212 (1974).
7. Colombo, M. & Gross, C. G. Responses of inferior temporal cortex and hippocampal neurons during delayed matching to sample in monkeys (Macaca fascicularis). *Behav Neurosci* **108**, 443–455 (1994).
8. Kamiński, J. *et al.* Persistently active neurons in human medial frontal and medial temporal lobe support working memory. *Nat Neurosci* **20**, 590–601 (2017).
9. Solomon, P. R., Vander Schaaf, E. R., Thompson, R. F. & Weisz, D. J. Hippocampus and trace conditioning of the rabbit's classically conditioned nictitating membrane response. *Behav Neurosci* **100**, 729–744 (1986).
10. Curtis, C. E. & Lee, D. Beyond working memory: the role of persistent activity in decision making. *Trends Cogn Sci* **14**, 216–222 (2010).
11. Pastalkova, E., Itskov, V., Amarasingham, A. & Buzsáki, G. Internally generated cell assembly sequences in the rat hippocampus. *Science* **321**, 1322–1327 (2008).
12. MacDonald, C. J., Lepage, K. Q., Eden, U. T. & Eichenbaum, H. Hippocampal 'time cells' bridge the gap in memory for discontiguous events. *Neuron* **71**, 737–749 (2011).
13. Time cell sequences during delay intervals are not dependent on brain state and do not support hippocampus-dependent working memory | Nature Communications. https://www.nature.com/articles/s41467-025-62498-z.
14. Forbes, A. *Physiology of the Nervous System* . By J. F. Fulton. London, New York, Toronto: Oxford University Press, 1938. Pp. xv + 675. *Science* **90**, 17–18 (1939).
15. Hebb, D. O. *The Organization of Behavior; a Neuropsychological Theory*. xix, 335 (Wiley, Oxford, England, 1949).
16. Compte, A. Computational and in vitro studies of persistent activity: edging towards cellular and synaptic mechanisms of working memory. *Neuroscience* **139**, 135–151 (2006).
17. Burak, Y. & Fiete, I. R. Fundamental limits on persistent activity in networks of noisy neurons. *Proc Natl Acad Sci U S A* **109**, 17645–17650 (2012).
18. Hasselmo, M. E. & Sarter, M. Modes and models of forebrain cholinergic neuromodulation of cognition. *Neuropsychopharmacology* **36**, 52–73 (2011).
19. Egorov, A. V., Hamam, B. N., Fransén, E., Hasselmo, M. E. & Alonso, A. A. Graded persistent activity in entorhinal cortex neurons. *Nature* **420**, 173–178 (2002).

20. Knauer, B., Jochems, A., Valero-Aracama, M. J. & Yoshida, M. Long-lasting intrinsic persistent firing in rat CA1 pyramidal cells: a possible mechanism for active maintenance of memory. *Hippocampus* **23**, 820–831 (2013).
21. Andrade, R. Cell excitation enhances muscarinic cholinergic responses in rat association cortex. *Brain Research* **548**, 81–93 (1991).
22. Fraser, D. D. & MacVicar, B. A. Cholinergic-Dependent Plateau Potential in Hippocampal CA1 Pyramidal Neurons. *J. Neurosci.* **16**, 4113–4128 (1996).
23. Klink, R. & Alonso, A. Muscarinic Modulation of the Oscillatory and Repetitive Firing Properties of Entorhinal Cortex Layer II Neurons. *Journal of Neurophysiology* **77**, 1813–1828 (1997).
24. Krnjević, K., Pumain, R. & Renaud, L. The mechanism of excitation by acetylcholine in the cerebral cortex. *J Physiol* **215**, 247–268 (1971).
25. Arboit, A., Reboreda, A. & Yoshida, M. Involvement of TRPC4 and 5 Channels in Persistent Firing in Hippocampal CA1 Pyramidal Cells. *Cells* **9**, 365 (2020).
26. Fransen, E., Alonso, A. A. & Hasselmo, M. E. Simulations of the role of the muscarinic-activated calcium-sensitive nonspecific cation current INCM in entorhinal neuronal activity during delayed matching tasks. *J Neurosci* **22**, 1081–1097 (2002).
27. Hasselmo, M. E. Grid cell mechanisms and function: contributions of entorhinal persistent spiking and phase resetting. *Hippocampus* **18**, 1213–1229 (2008).
28. Camperi, M. & Wang, X. J. A model of visuospatial working memory in prefrontal cortex: recurrent network and cellular bistability. *J Comput Neurosci* **5**, 383–405 (1998).
29. Fall, C. P. & Rinzel, J. An intracellular Ca2+ subsystem as a biologically plausible source of intrinsic conditional bistability in a network model of working memory. *J Comput Neurosci* **20**, 97–107 (2006).
30. Goldman, M. S., Levine, J. H., Major, G., Tank, D. W. & Seung, H. S. Robust persistent neural activity in a model integrator with multiple hysteretic dendrites per neuron. *Cereb Cortex* **13**, 1185–1195 (2003).
31. Lin, C., Sherathiya, V. N., Oh, M. M. & Disterhoft, J. F. Persistent firing in LEC III neurons is differentially modulated by learning and aging. *Elife* **9**, e56816 (2020).
32. Glasgow, S. D. *et al.* Acetylcholine synergizes with netrin-1 to drive persistent firing in the entorhinal cortex. *Cell Reports* **43**, 113812 (2024).
33. Olton, D. S., Becker, J. T. & Handelmann, G. E. Hippocampus, space, and memory. *Behavioral and Brain Sciences* **2**, 313–365 (1979).
34. Nadel, L. & MacDonald, L. Hippocampus: cognitive map or working memory? *Behavioral and Neural Biology* **29**, 405–409 (1980).
35. Sabariego, M. *et al.* Time Cells in the Hippocampus Are Neither Dependent on Medial Entorhinal Cortex Inputs nor Necessary for Spatial Working Memory. *Neuron* **102**, 1235-1248.e5 (2019).
36. Ito, H. T., Zhang, S.-J., Witter, M. P., Moser, E. I. & Moser, M.-B. A prefrontal–thalamo–hippocampal circuit for goal-directed spatial navigation. *Nature* **522**, 50–55 (2015).
37. Durstewitz, D., Seamans, J. K. & Sejnowski, T. J. Neurocomputational models of working memory. *Nat Neurosci* **3**, 1184–1191 (2000).
38. Khona, M. & Fiete, I. R. Attractor and integrator networks in the brain. *Nat Rev Neurosci* **23**, 744–766 (2022).
39. Taube, J. S. & Bassett, J. P. Persistent neural activity in head direction cells. *Cereb Cortex* **13**, 1162–1172 (2003).
40. McNaughton, B. L., Battaglia, F. P., Jensen, O., Moser, E. I. & Moser, M.-B. Path integration and the neural basis of the ‘cognitive map’. *Nat Rev Neurosci* **7**, 663–678 (2006).

41. Saber Marouf, B. *et al.* TRPC4 Channel Knockdown in the Hippocampal CA1 Region Impairs Modulation of Beta Oscillations in Novel Context. *Biology (Basel)* **12**, 629 (2023).
42. Goldman-Rakic, P. S. Cellular basis of working memory. *Neuron* **14**, 477–485 (1995).
43. Spellman, T. *et al.* Hippocampal-prefrontal input supports spatial encoding in working memory. *Nature* **522**, 309–314 (2015).
44. A prefrontal-thalamo-hippocampal circuit for goal-directed spatial navigation - PubMed. https://pubmed.ncbi.nlm.nih.gov/26017312/.
45. Athanasiadis, M. *et al.* Low rate hippocampal delay period activity encodes behavioral experience. *Hippocampus* **34**, 422–437 (2024).
46. Quirk, C. R. *et al.* Precisely timed theta oscillations are selectively required during the encoding phase of memory. *Nat Neurosci* **24**, 1614–1627 (2021).
47. Loewenstein, Y. *et al.* Bistability of cerebellar Purkinje cells modulated by sensory stimulation. *Nat Neurosci* **8**, 202–211 (2005).
48. Bröker-Lai, J. *et al.* Heteromeric channels formed by TRPC1, TRPC4 and TRPC5 define hippocampal synaptic transmission and working memory. *EMBO J* **36**, 2770–2789 (2017).
49. Lepannetier, S. *et al.* Activation of TRPC1 Channel by Metabotropic Glutamate Receptor mGluR5 Modulates Synaptic Plasticity and Spatial Working Memory. *Front Cell Neurosci* **12**, 318 (2018).
50. Vogel, P., Hahn, J., Duvarci, S. & Sigurdsson, T. Prefrontal pyramidal neurons are critical for all phases of working memory. *Cell Rep* **39**, 110659 (2022).
51. Leis, T., Pallage, V., Toniolo, G. & Will, B. Working memory theory of hippocampal function needs qualification. *Behavioral and Neural Biology* **42**, 140–157 (1984).
52. Cacucci, F., Yi, M., Wills, T. J., Chapman, P. & O'Keefe, J. Place cell firing correlates with memory deficits and amyloid plaque burden in Tg2576 Alzheimer mouse model. *Proc Natl Acad Sci U S A* **105**, 7863–7868 (2008).
53. Amaral, D. G. Emerging principles of intrinsic hippocampal organization. *Curr Opin Neurobiol* **3**, 225–229 (1993).
54. Couey, J. J. *et al.* Recurrent inhibitory circuitry as a mechanism for grid formation. *Nat Neurosci* **16**, 318–324 (2013).
55. Miller, E. K., Erickson, C. A. & Desimone, R. Neural mechanisms of visual working memory in prefrontal cortex of the macaque. *J Neurosci* **16**, 5154–5167 (1996).
56. Noorman, M., Hulse, B. K., Jayaraman, V., Romani, S. & Hermundstad, A. M. Maintaining and updating accurate internal representations of continuous variables with a handful of neurons. *Nat Neurosci* **27**, 2207–2217 (2024).
57. Jochems, A. & Yoshida, M. A robust in vivo-like persistent firing supported by a hybrid of intracellular and synaptic mechanisms. *PLoS One* **10**, e0123799 (2015).
58. Gothard, K. M., Skaggs, W. E., Moore, K. M. & McNaughton, B. L. Binding of hippocampal CA1 neural activity to multiple reference frames in a landmark-based navigation task. *J Neurosci* **16**, 823–835 (1996).
59. Ballinger, E. C., Ananth, M., Talmage, D. A. & Role, L. W. Basal Forebrain Cholinergic Circuits and Signaling in Cognition and Cognitive Decline. *Neuron* **91**, 1199–1218 (2016).
60. Wang, M. *et al.* Neuronal basis of age-related working memory decline. *Nature* **476**, 210–213 (2011).
61. Martin, M. M. & Wallace, D. G. Selective hippocampal cholinergic deafferentation impairs self-movement cue use during a food hoarding task. *Behav Brain Res* **183**, 78–86 (2007).

554 62. Croxson, P. L., Kyriazis, D. A. & Baxter, M. G. Cholinergic modulation of a specific
555 memory function of prefrontal cortex. *Nat Neurosci* **14**, 1510–1512 (2011).
556 63. Puram, S. V. *et al.* A TRPC5-regulated calcium signaling pathway controls dendrite
557 patterning in the mammalian brain. *Genes Dev* **25**, 2659–2673 (2011).
558 64. Kadir, S. N., Goodman, D. F. M. & Harris, K. D. High-dimensional cluster analysis
559 with the masked EM algorithm. *Neural Comput* **26**, 2379–2394 (2014).
560 65. Hattori, S., Chen, L., Weiss, C. & Disterhoft, J. F. Robust hippocampal responsivity
561 during retrieval of consolidated associative memory. *Hippocampus* **25**, 655–669 (2015).
562 66. Skaggs, W., McNaughton, B. & Gothard, K. An Information-Theoretic Approach to
563 Deciphering the Hippocampal Code. in *Advances in Neural Information Processing Systems*
564 (eds Hanson, S., Cowan, J. & Giles, C.) vol. 5 (Morgan-Kaufmann, 1992).
565 67. Guardamagna, M., Stella, F. & Battaglia, F. P. Heterogeneity of network and coding
566 states in mouse CA1 place cells. *Cell Rep* **42**, 112022 (2023).
567 68. McHugh, T. J., Blum, K. I., Tsien, J. Z., Tonegawa, S. & Wilson, M. A. Impaired
568 Hippocampal Representation of Space in CA1-Specific NMDAR1 Knockout Mice. *Cell* **87**,
569 1339–1349 (1996).
570

571

572

573

574

575 # Tables

576

577 **Table 1. Comparisons of passive membrane properties**

	RMP (mV)	Resistance (MOhm)	Adaptation Index	Intrinsic Excitability (Hz)			
				50 pA	100 pA	150 pA	200 pA
Non-injected	-64.19 ± 0.18	163.31 ± 4.82	0.43 ± 0.02	5.09 ± 0.48	20.45 ± 0.69	29.55 ± 0.71	39 ± 0.54
Scrambled	-64.20 ± 0.21	180.66 ± 2.72	0.53 ± 0.02	2.5 ± 0.35	13.71 ± 0.56	25.21 ± 0.64	33.21 ± 0.82
TRPC4 KD	-63.79 ± 0.25	173.85 ± 2.62	0.67 ± 0.03	7.86 ± 0.49	*22.71 ± 0.59	30.5 ± 0.70	36.57 ± 0.65

578

579 RMP: resting membrane potential, Resistance: input resistance, Adaptation index: firing rate adaptation

580 index.

581

582

583 # Methods

584 **Animals**

585 Twelve-week-old C57BL6/J male mice were obtained from a local animal facility. The mice were
586 group-housed until the time of surgery and individually housed thereafter to avoid injury to sutures
587 and/or implants. A 12-h light/dark cycle was used, and the mice underwent experiments during the light
588 cycle. Mice housing room conditions were maintained at 21–24°C and 40–50% humidity. All
589 experimental procedures were performed in accordance with animal research permission (TVA)
590 obtained from the animal committee of Sachsen-Anhalt (Landesverwaltungsamt Referat
591 Verbraucherschutz, Veterinärangelegenheiten, Az. 42502-2-1388 DZNE, 203.m-42502-2-1665
592 DZNE).

593

594 **TRPC4 channel knockdown**

595 We developed a TRPC4 shRNA-expressing virus (TRPC4_AAV_U6_shRNA2_GFP) to knock down
596 TRPC4 channels and a scramble virus (AAV_U6_scramble_GFP) for the control experiments. Oligos
597 for TRPC4 were designed based on Puram and colleagues[63] and were ordered from Sigma-Aldrich. The
598 following oligonucleotides were used to clone siRNA against mTRPC4 into AAV_U6_GFP:

599 mTRPC4_siRNA2: siRNA_TRPC4_Mouse/Human_2: Sense and antisense

600 5'- GATCC GGTCAGACTTGAACAGGCAA TTCAAGAGA

601 TTGCCTGTTCAAGTCTGACC TTTTTTG – 3'

602 3'- G CCAGTCTGAACTTGTCCGTT AAGTTCTCT AAC-GGACAAGTTCAGACTGG

603 AAAAAACTTAA-5'

604 Adeno-associated virus (AAV2) and U6 were used as the vectors and promoters, respectively. After
605 purification, the titers were checked by qPCR (using TaqMan probes) and different dilutions. The titer
606 for TRPC4_AAV_U6_shRNA2_GFP was $4.03*10^{12}$ and for AAV_U6_scramble_GFP was $3.56*10^{12}$.
607 Finally, primary hippocampal cell cultures were infected with either no virus, scrambled virus, or
608 TRPC4 KD virus, and a significant reduction in TRPC4 mRNA expression by the TRPC4 KD virus

609 was confirmed by RT-qPCR (Fig. 1A).

610

611 **Surgery**

612 C57BL/6JCrl male mice were weighed and anesthetized using a ketamine and xylazine cocktail
613 (ketamine 20 mg/mL + xylazine 2.5 mg/mL, 0.1 mL/20 g). The head was fixed in the stereotactic device
614 approximately 10 min after anesthetic injection. Head hair was completely removed, and the head was
615 scrubbed using betadine (povidone-iodine) and ethanol 70%. A small incision was made using a scalpel,
616 and the tissues were gently retracted. The skull position was checked horizontally. The Bregma point
617 was used as reference, and the injection sites were marked according to coordinates from Paxinos atlas
618 (AP: -2.1, ML±1.7, DV: 1.1 and AP: -2.7, ML±2.5, DV: 1.5). The marked points were drilled with a
619 0.7 mm drill tip. TRPC4_AAV_U6_shRNA2_GFP or AAV_U6_scramble_GFP viral particles were
620 injected using a Hamilton neuro syringe (1701, 33 g needle) and stereotaxic syringe pump (CHEMYX,
621 NANOJET) to control injection speed (100 nL/min) and volume (1 uL/site). The needle remained at the
622 injection site for 5 min before retraction. Next, the skin was closed using veterinary surgery glue, and
623 carprofen (5 mg/kg) was subcutaneously injected. Metamizole (200 mg/kg) was added to a 100 mL
624 water bottle. The mice were allowed to recover for a few hours in the surgery room and then transferred
625 to the animal room. They were checked daily (for three days) for recovery and pain management.
626 For *in vivo* electrophysiological experiments, a microdrive with eight tetrodes was implanted on the
627 right hemisphere and lateral to the virus injection site (AP: -2.1, ML±1.8, DV: 0.6). Four anchor screws
628 and one ground screw are affixed to the skull. The implant was fixed using acrylic dental cement.

629

630 ***In vitro* neural recordings**

631 The mice were deeply anesthetized with isoflurane, and the brains were quickly extracted after
632 decapitation. Brains were placed in ice-cold cutting solution (110 mM) 110 Choline Cl, 7 mM MgCl2
633 (6H2O), 0.5 CaCl2, 2.5 KCl, 25 glucose, 1.2 NaH2PO4, 25 mM NaHCO3, 3 mM pyruvic acid, 11.5
634 ascorbic acid, and 100 mM D-mannitol). A Leica VT-1000 vibratome was used to obtain 350 μM
635 coronal slices. Brain slices were transferred to a holding chamber containing normal ACSF (nACSF)
636 (126 mM) (126 mM NaCl, 1.2 mM NaH2PO4, 26 mM NaHCO3, 1.5 mM MgCl2, 1.6 mM CaCl2, 3

637 mM KCl, and 10 mM glucose). Slices were submerged for 30 min at 37 °C and then transferred to
638 another holding chamber at room temperature for at least 30 min before recording.
639 Brain slices were transferred to the recording chamber and continuously superfused with
640 nACSF (34.5 ± 1.5°C). The cells were visualized using an upright microscope (Olympus BX51WI)
641 with a 40x water immersion objective and a Thorlabs CS895MU monochrome camera. GFP+ cells were
642 located by exciting GFP with a 470 nm wavelength LED (CoolLED PE 4000) through a filter cube with
643 excitation filter 469 ± 17.5 nm, dichroic 452–490 nm / 505–800 nm, and emission filter 525 ± 19.5 nm.
644 Whole-cell configuration was achieved using 3–5 MΩ patch pipettes filled with intracellular solution
645 (in mM: 120 K-gluconate, 10 HEPES, 0.2 EGTA, 20 KCl, 2 MgCl2, 7 PhCreat di(tris), 4 Na2ATP, and
646 0.3 Tris-GTP (pH adjusted to 7.3 with KOH). For labeling purposes, 0.1% biocytin was added to the
647 intracellular solution. Access resistance was monitored and compensated for several times during
648 recording. The liquid junction potential was not corrected. Electrophysiological signals were amplified
649 using a Multiclamp 700A amplifier and digitized using an Axon Digidata 1550 B. Current clamp
650 recordings were routinely filtered at 10 KHz and sampled at 20 KHz using pClamp 11 software. After
651 recording, the slices were stored at 4°C in a phosphate-buffered saline (PBS) solution with 4%
652 paraformaldehyde (PFA).
653
654 **Behavioral task**
655 The spatial working memory task in the T-maze was started four weeks after virus injection. Before this
656 test, the mice were handled for three days to habituate to the experimenter. Mice were food-deprived at
657 the start of handling to motivate them for the reward, and reward pellets were introduced to them before
658 starting the main experiment. Animal weight was maintained between 85–90% of body weight before
659 food deprivation. Second, habituation to the T-maze (OHARA Ltd., Japan) was performed for three
660 days.
661 Each animal was tested for 10 days, with each day constituting 10 trials (10 sample +10 choice
662 phases). Each trial started with a sample trial (forced trial), in which the T-maze software assigned the
663 left or right door (at the T-junction) to open randomly. First, the start door was opened, and the mouse
664 moved from the start area to the stem, open arm (top of the T-maze), and goal area where it received

665 the reward. Next, the animal returned to the start area using the return arm and waited for 30 s (delay
666 period). After the delay, the choice trial began; this time, both the left and right arms were open, and
667 the mouse chose the arm opposite the sample trial. If the trial was successful, the animal received a
668 pellet at the goal location. After collecting the reward, the animal moved back to the start area, where a
669 new trial began after 45 s (inter-trial interval, ITI). After each experiment, the maze floor was cleaned
670 with 10% ethanol, and the walls were cleaned with water. Behavioral data were analyzed using
671 MATLAB (MathWorks) and SPSS (GEE).
672
673 ***In vivo* neural recordings**
674 Tetrodes were made using 12.5 μm Tungsten wire (California Fine Wire Co.) and grouped in a single
675 bundle with eight tetrodes (32 channels) inside a microdrive (AXONA). The tetrodes were gold-plated
676 using nanoZ (White Matter LLC, USA) in gold solution to reduce the impedance to 150 kΩ.
677 Screening was conducted 7–10 days after surgery and after handling the animals to place the
678 tetrodes in the pyramidal layer of CA1. Screening was performed in an open-field arena (30 × 30 cm,
679 shielded and grounded). The presence of place cells, autocorrelation, firing frequency, and waveform
680 characteristics were the criteria used to identify the pyramidal layer. Once the tetrodes were in a position
681 or very close to CA1, the behavioral experiment in the T-maze began.
682 Single-unit activity and local field potentials (LFP) were recorded using an in vivo
683 electrophysiology setup (Axona Ltd.). The data were recorded in the raw mode at a sampling rate of 48
684 kHz. To obtain single-unit spike data, raw data were referenced and band-passed (400–8000 Hz) using
685 custom scripts written in MATLAB (MathWorks), and spikes were detected using TINT (Axona Ltd.).
686 The detected spikes were clustered using KlustaKwik[64] for automatic clustering, and manual curation
687 of the clusters was performed using the Klusters software (Lynn Hazan). LFP data with a 4800 Hz
688 sampling rate were created using TINT (Axona Ltd.). The position of the mouse was tracked at 50 Hz
689 using a video camera that recorded the position of a light-emitting diode attached to the mouse head.
690
691 **Histology**

692 Mice were anesthetized with a ketamine and xylazine cocktail and transcardially perfused with cold
693 PBS (4°C, 15 mL) and then cold paraformaldehyde 4% (PFA, PH~7.4, 50 mL). Brains were removed
694 and post-fixed in PFA 4% at 4°C for 24 h. After applying the cryoprotective protocol (one day in sucrose
695 10%, three days in sucrose 30%), samples were embedded in cubic molds filled with Optimal Cutting
696 Temperature compound (O.C.T.) and then snap frozen. Next, the samples were transferred to the -80°C
697 freezer for storage. The fixed samples were sectioned using a cryostat. The slices were then covered
698 and mounted using a mounting medium. Images were obtained with a confocal microscope (Zeiss,
699 AxioImager M2) and fluorescence microscope (Keyence, BZ-X710) using 2.5x, 5x, and 40x objectives
700 to control for virus expression and tetrode traces (Supplemental Fig. 1).
701
702 ***In vitro* data analysis**
703 The resting membrane potential was measured by averaging the membrane potential for 1 min after seal
704 opening without current injection. Input resistance was calculated using Ohm's law, measuring the
705 voltage deflection in response to a negative current pulse of -50 pA at -65 mV. Intrinsic excitability was
706 evaluated by counting the number of action potentials during the positive step-wise current injections
707 (1 s), from -300 to 300 pA in 50 pA jumps (IV protocol). The adaptation index was calculated by
708 dividing the instantaneous frequency of the last pair of action potentials by the instantaneous frequency
709 of the second pair of action potentials in the first sweep, with at least 10 action potentials in the IV
710 protocol. *In vitro* persistent firing was induced by a 2 s 100 pA current injection at a voltage level of 5–
711 3 mV below the action potential threshold. The strength of persistent firing was evaluated by calculating
712 the average firing frequency and depolarization in the first 10 s post-stimulus. The cells were classified
713 as having long (> 30 s), short (< 30 s), or no persistent firing, based on the duration of persistent firing
714 observed (measured from the offset of the stimulus).
715
716 ***In vivo* data analysis**
717 The data were analyzed using custom-written MATLAB scripts and the CMBHome toolbox developed
718 at the Center for Memory and Brain, Boston University.
719

720 *Temporal binning and Z-score firing rate*

721 The time-binned firing rate of each cell was prepared using a 0.5 s bin and smoothed with a 2.5 s
722 Gaussian window to analyze *in vivo* persistent firing. The Z-scored firing rate was calculated from the
723 time-binned firing rate data using the following equation:

724 $$Z = (f - mean(F))/std(F),$$

725 where *f* and F are the binned firing rates from the period of interest and baseline period, respectively.

726

727 *Cell type classification based on activity change*

728 Neurons were classified into activated (Act), suppressed (Sup), and non-modulated (NM) cells,
729 according to the delay period activity[65] (Fig. 2E). The binned firing rate at baseline (15–5 s before the
730 delay) was compared to the activity during the delay (0–25 s) using the Wilcoxon rank-sum test (WRS).
731 Cells were considered to be modulated if the test result was significant ($p < 0.01$). The z-value obtained
732 during the test (WRS z-value) was used to classify the modulated cells into the Act (WRS z-value >
733 2.58) and Sup (WRS z-value < -2.58) groups. The remaining cells were classified as NM. The WRS z-
734 values were used to plot a histogram, as shown in Fig. 2E.

735

736 *Temporal field*

737 The peak z-scored firing rate during the delay period was determined to define the temporal field for
738 each cell. The temporal field duration was defined as the time when the z-scored firing rate was
739 continuously above 10% of the peak value (Fig. 2I). In Fig. 3, the temporal field duration is defined in
740 the same way, using the raw firing rate instead of the z-scored firing rate.

741

742 *SVM analysis*

743 A population vector was built for each trial of each session using neuronal activity during the delay
744 period (0–25 s) or from the goal area (0–10 s). Single-unit spike activity was temporarily binned (0.5 s
745 bin) for left vs. right and ITI vs. delay comparisons. A temporal bin size of 0.02 s was used for the left
746 vs. right goal comparison with a 5 s sliding window (Fig. 7F and G). Each trial was then labeled

747 according to the type of test: ITI vs. delay or left vs. right (retrospective or prospective). Only sessions
748 with at least 15 units were included in the analysis.

749 Binary SVM comparisons were performed for each session with the fitcsvm function
750 (MATLAB) using a linear kernel and two-fold cross-validation of the input data to evaluate model
751 performance. The model was run 30 times, and the obtained balanced accuracies were averaged. To
752 evaluate the significance of the prediction, the class labels were scrambled, and the SVM model was
753 run for the non-scrambled data a minimum of 30 times (sessions where label permutation did not
754 generate at least 30 different combinations were not included in the analysis). Moreover, a random
755 accuracy distribution was built and then used to determine the z-scored balance accuracy. Sessions with
756 z-score > 1.96 were considered to have above-chance accuracy.

757

758 *Spatial information and place cells*

759 Spatial information (SI) is defined as the extent to which the firing of a cell can be used to predict the
760 position of the animal. The SI was calculated using the formula of Skaggs et al. (1992)[66]:

761 $$SI = \int_{\infty} \lambda(x) log_2 \frac{\lambda(x)}{\lambda} p(x) dx,$$

762 where SI is the information rate in bits/s, x is the spatial location of the animal, λ(x) is the mean
763 frequency at location x, p(x) is the probability of finding the animal at a given location in the maze, and
764 λ is the overall firing rate of the cell.

765 Spatially modulated cells were selected by building a randomized distribution of spatial
766 information values obtained by circularly shifting the spike timing and position vectors for at least 20 s
767 100 times. Cells with spatial information above the top 95% of the random distribution were considered
768 spatially modulated cells (place cells).

769 The spatial rate maps represent the average firing rate of a cell at a given location, and were
770 obtained by dividing the number of spikes at a location by the total time that the animal spent at that
771 location (occupancy). Rate maps were calculated using 1x1 cm bins, and the data were smoothed using
772 a two-dimensional convolution with a Gaussian kernel with a 2.5 cm standard deviation. Only bins with
773 speed greater than 2.5 cm/s were considered in the calculation.

774 Place field centers were detected as follows. First, pixels of a rate map with a high firing rate
775 (> 4 SD) were extracted. Extracted rate map was processed with the regionprops function (MATLAB)
776 to detect and characterize the individual fields and the area and centroid parameters were obtained. To
777 avoid detecting noise, fields smaller than 12 or larger than 650 cm^2 were discarded, and firing field with
778 the highest coefficient of variation was considered the main firing field of a given neuron. The
779 coefficient of variation was calculated as follows:
780

781 $$CV = \frac{Mean\ field\ firing\ rate}{SD\ field\ firing\ rate}$$

782

783 *Theta amplitudes*

784 Theta components were extracted by bandpass filtering of the LFP data (6-10 Hz). The theta amplitude
785 was calculated using the absolute value of the Hilbert transform of the filtered signal.
786

787 *Putative cell type classification*

788 Putative pyramidal neurons and interneurons were identified based on the average firing rate and spike
789 duration. Cells with an average firing rate < 8 Hz and a peak-to-peak spike duration > 0.255 ms were
790 classified as putative pyramidal cells, whereas those with an average firing rate > 8 Hz and a peak-to-
791 peak spike duration < 0.255 ms were classified as putative interneurons[67,68].
792

793 *Trial selection for goal analysis*

794 The duration of time animals stayed at the goal areas varied greatly from trial to trial, ranging from 1.6
795 to 410.0 s (median duration: 47.74 and 47.73 s for control and TRPC4 KD groups, respectively; WRS
796 test, p = 0.99), because the task did not restrict the time animals spend at the goal areas. In addition, the
797 animals returned to the top arm (top of T) in some trials. Therefore, we limited our goal analysis to trials
798 in which the animals continuously spent at least 10 s within the goal area during the sample phase.
799 When multiple such periods were found in a trial, we analyzed the first incident. The baseline period to
800 build the z-scored firing rate was the last 20 s of the ITI period before goal entry. This ensured that goal

activity was not included in the baseline period. In Fig. 7A, H, and K, the black vertical gap separates the first 10 s, which is referenced to the end of the ITI period, from the rest, which is referenced to the start of goal entry. The trials in each recording session were first divided into left and right sample goal trials to compare correct and incorrect trial activities. Subsequently, we checked whether at least one correct or incorrect trial was present for each goal location. Sessions that did not meet these criteria were excluded from the analysis.

Bayesian position decoding

For Bayesian position decoding, we included sessions with at least 30 simultaneously recorded CA1 units. In each session, position decoding was performed on trials in which the mouse stayed at the goal location for longer than 10 s because our focus was on the maintenance of spatial representation over time. In each trial, position decoding was performed using a 12-s window spanning 4 s before to 8 s after goal entry (goal window). To build spatial tuning curves for later decoding, two-dimensional rate maps with a 1.7 cm spatial bin size were calculated for all cells using the spike data from the complement of the goal window within the session (i.e., all spike data of the session excluding the goal window from corresponding trial). Data used for decoding in each goal window consisted of spike counts from all cells binned into non-overlapping 200 ms time bins ($\Delta t = 0.2$ s), which were smoothed across time using a Gaussian kernel (6-bin window).

Decoding assumed independent Poisson spiking across units, such that for each spatial bin (state) s with expected rate $\lambda_i(s)$ from the rate map, the log-likelihood of observing counts r_i in a time bin was computed as $\sum_i[r_i \log \lambda_i(s) - \lambda_i(s)\Delta t]$; rate-map values were floored at 10^{-6} Hz to ensure numerical stability. A uniform prior over spatial states was used, and the posterior over all spatial bins was obtained by combining log-likelihood and log-prior and normalizing each time bin.

Decoded position was taken as the maximum a posteriori (MAP) spatial bin and converted to x–y coordinates using bin centers; posterior marginals over x and y were additionally computed by summing the 2D posterior over the orthogonal dimension. Ground-truth x(t) and y(t) at each decoding time bin midpoint was obtained by linear interpolation of the tracked position and discretized into a

spatial bin center coodinate. Decoding accuracy was quantified as the Euclidean distance between decoded and ground-truth position at each time bin.

Statistical analysis

The data were checked for distribution and homogeneity before statistical analysis. Comparisons between groups were performed using the Wilcoxon rank-sum and Kruskal–Wallis tests. A t-test or analysis of variance (ANOVA) followed by Tukey's post-hoc test was used for normally distributed data. Multiple-comparison corrections were used where relevant. Categorical variables (group ratios) were compared using the chi-squared test or Fisher's exact test if any group had fewer than five items. Boxplots represent the median and upper and lower quartiles. Significance was expressed as follows: * $p < 0.05$, ** $p < 0.01$, and *** $p < 0.001$.

Data availability

Data used in the current study will be available on request to the corresponding authors.

Code availability

All source codes used in the current study will be available on request to the corresponding authors.

Acknowledgments

We would like to thank K. Jeffery, S. Leutgeb, J. Leutgeb, M. Brandon, and K. Allen for their help in establishing the *in vivo* electrophysiological recordings. We thank L. Leichert and O. Stork for their assistance and technical support, and M. Freichel for sharing the TRPC KO mice with us. We thank M. Hasselmo, B. McNaughton, T. McHugh and S. Remy for their valuable comments on this manuscript. This work was supported by the Federal State of Saxony-Anhalt and the European Structural and Investment Funds (ESF, 2014–2020, project number ZS/2016/08/80645), the Deutsche

Forschungsgemeinschaft projects YO177/4-1, YO177/4-3, and YO177/7-1 (to M.Y.), and the German Center for Neurodegenerative Diseases (to A.D.).

Author Contributions

Conceptualization and experimental design, M.Y. and M.S.; analysis, A.R., M.Y., and B.S.M.; investigation, B.S.M.; writing, M.Y. and A. R.; methodology, A.D. and R.K.; software, M.Y. and F.T.; funding acquisition, M.Y.; supervision, M.Y. and M.S.

Competing interests

The authors declare no competing interests.

Corresponding author

Correspondence and requests for materials should be addressed to motoharu.yoshida@lin-magdeburg.de.

869 **Supplemental Information**

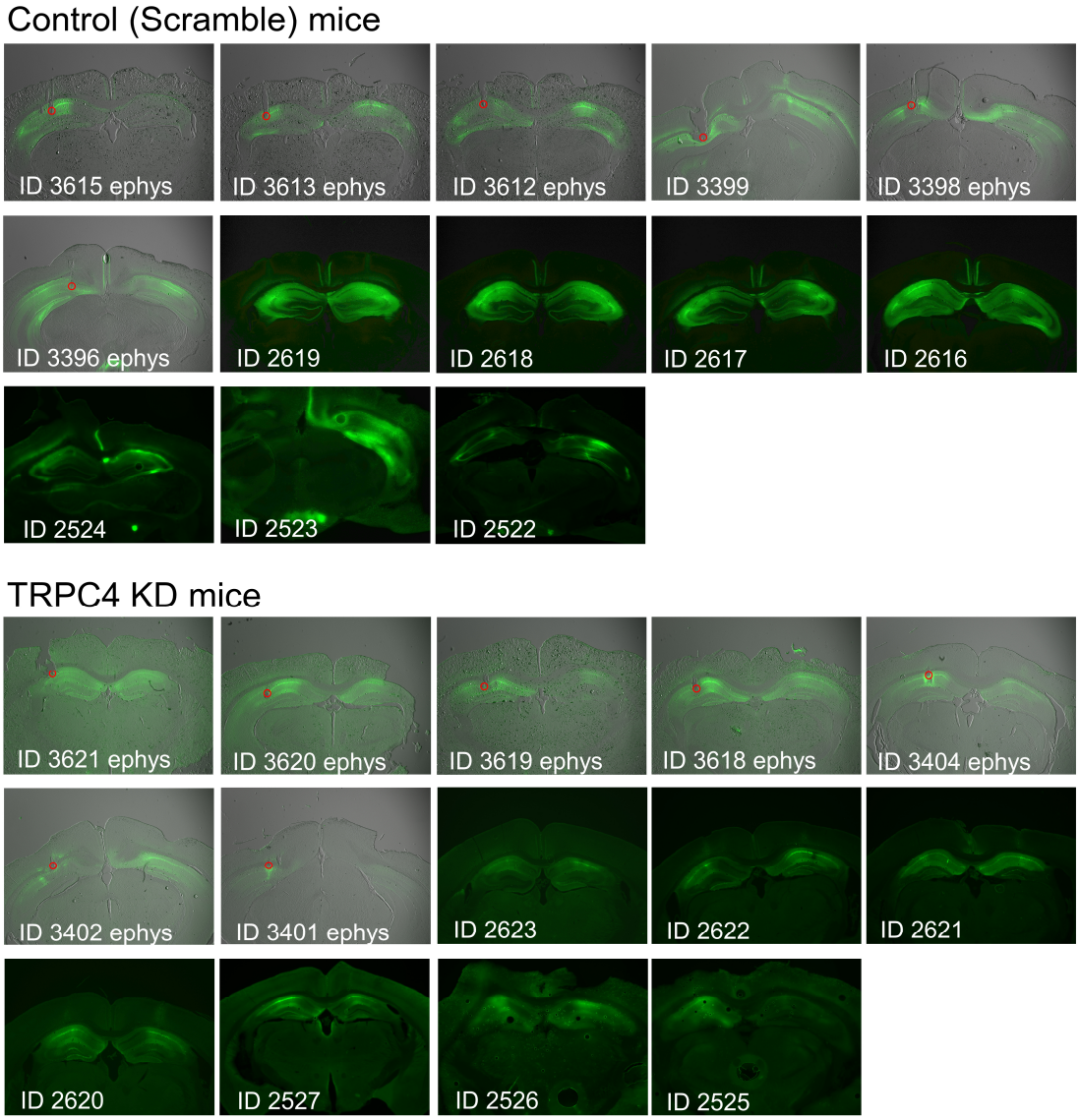

Supplemental Figure 1. Virus expression and tetrode track GFP expression and track locations of each animal for both the control and TRPC4 KD groups. Animal IDs followed by "ephys" indicate that those mice were used for electrophysiological recording. The tips of tracks are highlighted with a red circle. Other animals were only used for the behavioral test.

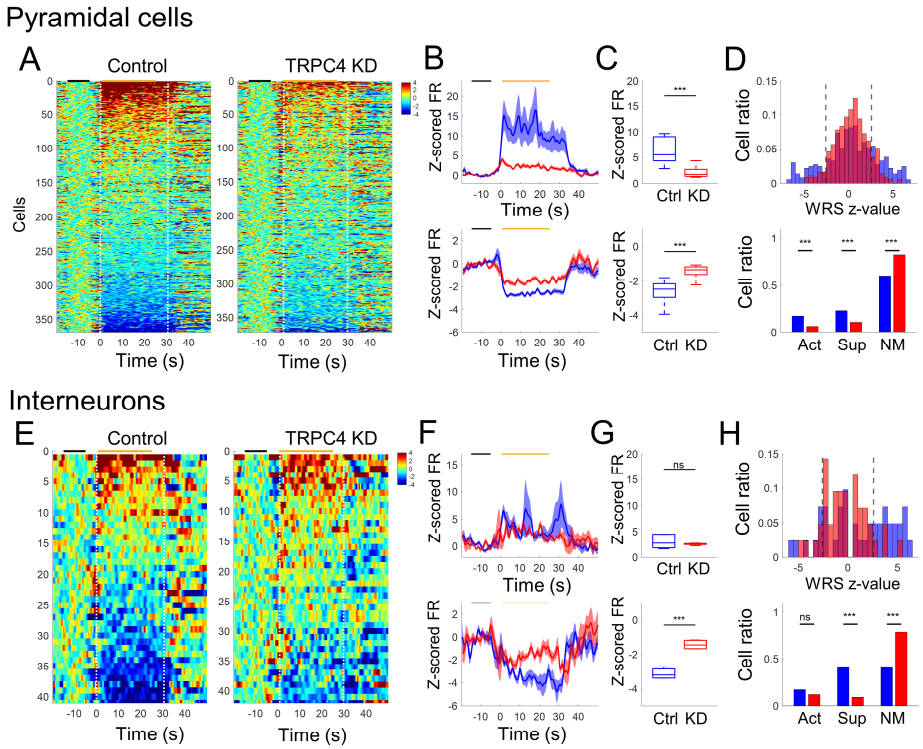

Supplemental Figure 2. Activity of putative pyramidal and interneurons (A) Z-scored firing rate of putative-pyramidal cells sorted by the delay period activity. Black and orange horizontal lines at the top of each panel indicate baseline period and period for cell sorting, respectively. (B) Averaged z-scored firing rate (FR) of top (upper panel) and bottom (lower panel) 10% cells in A. (C) Comparison of z-scored firing rate of the top (upper panel; Wilcoxon rank sum Test, $p < 0.001$) and bottom (lower panel; Wilcoxon rank sum test, $p < 0.001$) 10 % cells in A during the delay period (0-25 s). (D) Classification of activated (Act), suppressed (Sup) and non-modulated (NM) cells using Mann–Whitney U (MWU) test. The upper panel shows the distribution of Wilcoxon rank-sum z-values and the lower panel shows the ratio of cells in each category (WRS test, $p < 0.001$ for all groups). (E to H) Same as A to D but for putative-interneurons. Statistical tests in G: WRS test, $p = 0.6905$ in the upper panel, and $p < 0.001$ in the lower panel.

870

871

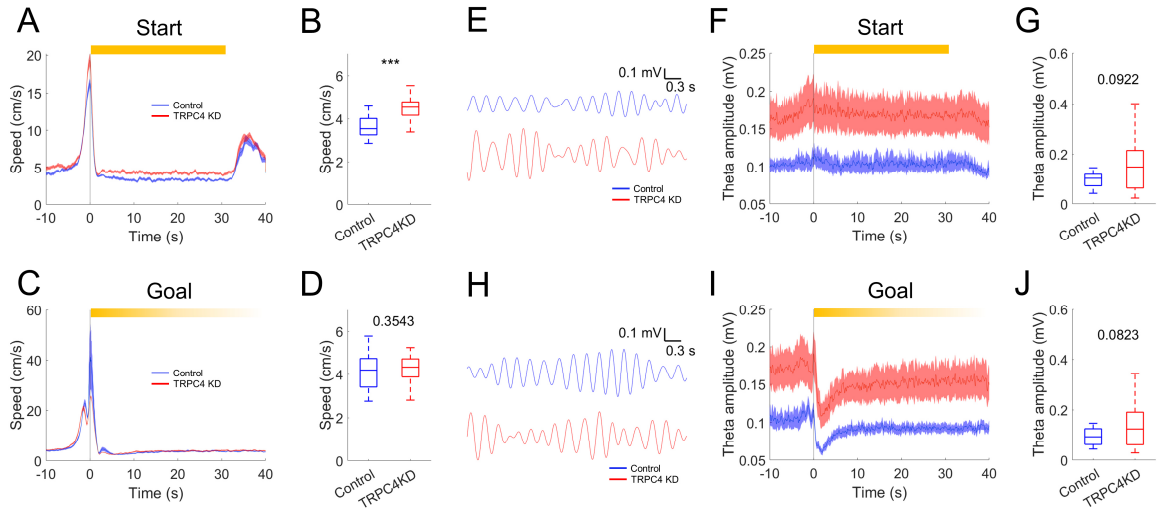

Supplemental Figure 3. Running speed and theta amplitude at the start and goal areas (A) Average running speed of control and TRPC4 KD animals at the start area. Time is relative to the entry to the start area. This figure includes both the sample (ITI) and choice (delay) phases. (B) Comparison of the speed in the start area (Wilcoxon rank sum test, $p < 0.001$). (C) Same as A but for the goal area. Note that there was no set duration during which animals stayed at the goal area. While we show 40 s of goal speed data, animals were already out of the goal areas in some trials. (D) Comparison of the speed in the goal area (Wilcoxon rank sum test, $p = 0.35$). For this comparison, the speed of each session was calculated using only the time the animal stayed in the goal area. (E) Examples of filtered theta oscillation at the start area. (F) Theta amplitudes of control and TRPC4 KD animals at the start area. (G) Comparison of the averaged theta amplitudes in the start area (Wilcoxon rank sum test, $p = 0.092$). (H) Examples of filtered theta oscillation at the goal area. (I) Theta amplitudes of control and TRPC4 KD animals at the goal area. As in C, animals were out of the goal areas in some trials before the end of the trace. (J) Comparison of the theta amplitudes in the goal area (Wilcoxon rank sum test $p = 0.082$). As in D, the theta amplitude of each session was calculated using only the time the animal stayed in the goal area.